MALAYSIAN JOURNAL OF SCIENCE

Vol. 38 • Special Issue (3) • 2019

University of Malaya – Indonesian Universities Symposium 2018 (UMInd 2018)

JURNAL SAINS MALAYSIA

MJS

ISSN 1394 - 3065

The Malaysian Journal of Science is indexed or cited in the following Scientific Databases: Elsevier Bibliographic Databases (ACI, Scopus, EMBASE, Compendex, GEOBASE, EMBiology, Elsevier BIOBASE, FLUIDEX and World Textiles); CAB Abstracts and Chemical Abstracts Service Database

http://www.myjurnal.my/public/browse-journal-view.php?id=194
www.mjs.um.edu.my

Selected papers from the

University of Malaya – Indonesian Universities Symposium 2018 (UMInd2018)

Kuala Lumpur, Malaysia. 8th - 9th November 2018.

We are honoured to bring you this compilation of carefully selected papers presented at the University of Malaya – Indonesian Universities Symposium 2018 (UMInd2018) that was held in Kuala Lumpur, Malaysia from 8th to 89h November 2018.

Science is a universal knowledge with important roles in various modern disciplines and human intellectual growth. Rapid development in technology and communication owes largely to the advancement in science. With the aspiration to develop frontier scientific knowledge, the Faculty of Science, University of Malaya (UM) is honored to organize the first "University of Malaya - Indonesian Universities Symposium" (UMInd 2018) thus bringing together scientists from various disciplines from University of Malaya and selected universities in Indonesia.

The primary focus of this conference was to to provide a conducive platform for leading academic scientists, researchers and research scholars in exchanging and sharing their experiences and ideas on current aspects of science. We also showcase discoveries, latest innovations and concepts that can be expanded in line with the theme of the symposium. UMInd2018 symposium also managed to promote interaction and potential research collaborations between researchers in Malaysia and Indonesia.

THE STUDY OF PLASMA PARAMETER AND THE EFFECT OF EXPERIMENT SET UP MODIFICATION BY USING MODELLING SOFTWARE

Ersyzario Edo Yunata[1a]*, Muhammad Ghufron[2b]

[1]Department of Science and Technology, Airlangga University, Surabaya, INDONESIA. E-mail: ersyzario.edo@fst.unair.ac.id[a]
[2]Department of Physics, Brawijaya University, Malang, INDONESIA. E-mail: mghufron@ub.ac.id[b]
*Corresponding Author: ersyzario.edo@fst.unair.ac.id
Submitted: 5th December 2018 Accepted: 21st August 2019 Published:30th November 2019
DOI: https://doi.org/10.22452/mjs.sp2019no3.1

ABSTRACT Plasma diagnosis has done by using Langmuir probe and software modeling. COMSOL and JMAG software were employed to characterize the electron density and identifying the set up effect in the plasma system. First, the COMSOL software was employed to simulate the behavior of electron density. The pressure and DC-bias voltage were varied during the simulation process. The DC bias voltage was varied in the range -200 V to -600V. The pressure was also varied in the range 30 to 80 Pa. The high electron density was generated in the high DC-bias voltage and high pressure by using simulation process. Second, the Langmuir probe was also employed to measure the behavior of electron density inside the actual plasma chamber. The DC-bias voltage and pressure were also varied in the range - 350V to – 650V and 60 Pa to 120 Pa, respectively. The experiment and modeling result were shown the same trend for the behavior of electron density. Third, the JMAG software was also utilized to characterize and modifying the set up in the plasma system. The electrode and DC bias was varied in the range 100 to 500 V and -100 to -500 V, respectively. The electric field distribution was concentrated in the electrode and DC-bias plate from the original set up. However, the electric field distribution was shifted to the center area after modification process. The modifications of experiment set up have provided the new way to confine the electric field. The high concentrated of electric field was effective to generate high plasma density.

Keywords: plasma, electron density, plasma modeling, electric field, and plasma diagnosis

1. INTRODUCTION

The plasma is considered to be the fourth state of matter, after the solid, liquids and gases and is generally visualized as an arc or discharge of bright fluorescent light. Physically, it is a partially or wholly ionized gas mixture containing reactive species, such as electrons, positive ions, negative ions, free radicals, excited or non-excited gas molecules and photon (Mandal et al., 2018). Nowadays, the plasma technology has been widely utilized in many sectors, such as medical (Dai et al., 2018), food packaging (Misra et al., 2019), aerospace (Kgoete et al., 2018), semiconductor (Fanelli et al., 2017), electrical sector (Zhao et al., 2017) and so on. In the industrial sector, there are two different modes of plasma such as thermal plasma or hot plasma and non-equilibrium or

cold plasma. Thermal plasma is produced at high pressure (>10 kPa) by means of direct (DC) or alternating current (AC) or radio frequency (RF) or microwave sources with temperature around 2000-20000K. Non-equilibrium plasmas are low-pressure plasma characterized by high electron temperature and low ion and neutral temperatures (Samal et al., 2017). The study and characterization of plasma are needed with the purpose to obtain the optimum condition during application and plasma processing. There are many ways to characterize the plasma. Langmuir probe is one of the ways to measure the plasma density (Meshcheryakova et al., 2015). Optical emission spectroscopy (OES) is effective to describe the population in the plasma (Li et al., 2018). Both diagnostics are direct measurement of the plasma. However, there is an indirect method to characterize the plasma, that is through modeling. The modeling simulation provides more understanding of the processes in the plasma (Brezmes et al., 2014).

In the present study, two modeling software and Langmuir probe device were employed to study the plasma. The COMSOL software and Langmuir probe were utilized to characterize the effect of electron density with pressure and DC-bias voltage. Furthermore, the JMAG software was employed to describe the electric field distribution in the present set up. A modification of experiment set up was also employed with the purpose to get the optimum condition and better result for plasma processing. The modeling result was compared with the previous Langmuir probe diagnostic results (Yunata et al., 2013).

2. EXPERIMENTAL PROCEDURE

The plasma modeling consisted of several parts. First, the COMSOL software was utilized to simulate the effect of pressure and DC-bias voltage variation in the electron density. Second, the Langmuir probe was utilized to measure the plasma density inside the chamber. Third, the JMAG software was employed to characterize the effect of electric field in the experiment set up.

2.1 Plasma modelling by using COMSOL software

The one dimension plasma modelling was built to simulate the electron density behaviour in the COMSOL software. The effect of pressure and DC-bias voltage in the electron density was the main discussion in this study. The schematic of plasma modelling is depicted in figure 1. The chamber was modelled with rectangular form. The chamber was grounded similar to the original plasma machine condition in the laboratory. The cathode was also modelled with rectangular form. The cathode was biased with negative voltage. In the DC-bias voltage variation, the voltage was varied in the range of -200 to -600 V. Next, the range of low gas pressure from 30 to 80 Pa was chosen to characterize its effect in the electron density in plasma. The secondary electrons were chosen as a mechanism to generate plasma. The plasma was generated inside the chamber. The detail of simulation condition was depicted in the table

Table 1. Plasma simulation condition by using COMSOL software.

Parameters	
DC-bias voltage	*-200 to -600 V*
Pressure	*30 to 80 Pa*
Temperature	*400 K*
Gas	*Argon*

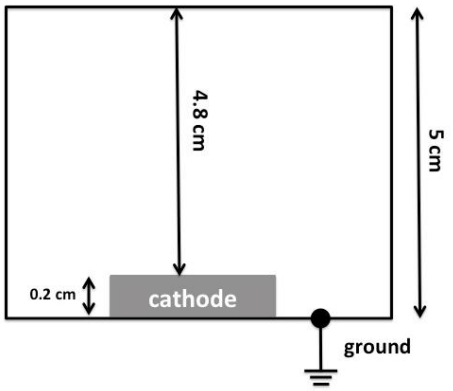

Figure 1. The schematic plasma modelling by using COMSOL software.

2.2 Langmuir Probe measurement process

Plasma parameter was measured with a single Langmuir probe analysis (Impedans ALP System). The schematic of the plasma system with Langmuir probe is depicted in figure 2. Details of probe specification are as follows: probe radius of 3.5×10^{-4} m, length of 0.01 m and resistance of 36 Ohm. The Langmuir probe was placed in the center of the chamber during the plasma processing. The electron density was measured at varying DC-bias and pressure. Then, the measured data were transferred and stored in the computer.

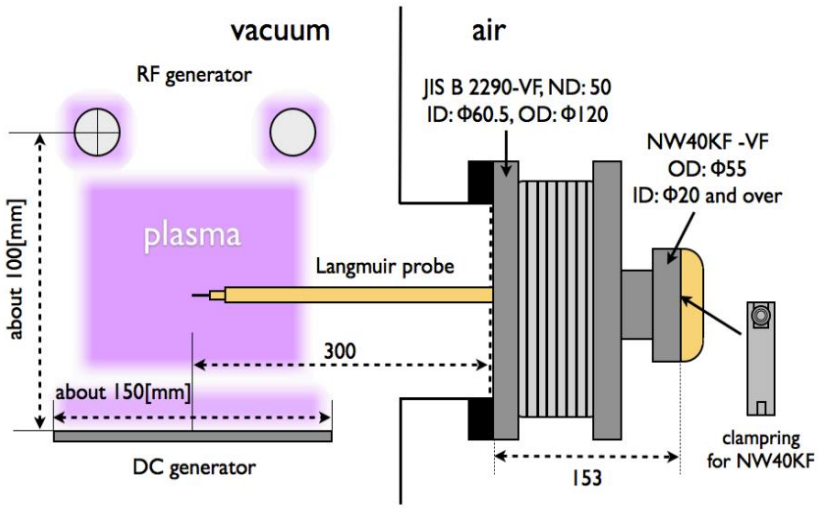

Figure 2. The schematic set up of Langmuir probe in plasma system

2.3 Plasma modelling by using JMAG software

The JMAG software was utilized to characterize the electric field distribution in the plasma system. The chamber was modelled with big circle form. The chamber was grounded as the actual plasma machine condition in laboratory. The electrode was also modelled with small circular form. The electrode was set with positive voltage from 100 to 500 V. The DC bias plate was modelled with rectangular form. The DC-bias plate was set with negative voltage. The DC-bias voltage was varied in the range -100 to -500 V. The schematic of JMAG simulation is depicted in figure 3. The voltage variation was done in the electrode and DC bias plate. The electric field was generated inside the chamber in this modelling result. The distribution of electric field was characterized in each variation. Modification to the experiment set up was also employed in this process in which the model of a metal conductor was inserted in the area between electrode and DC-bias plate. The simulation result was studied and applied in the real plasma processing system in the laboratory.

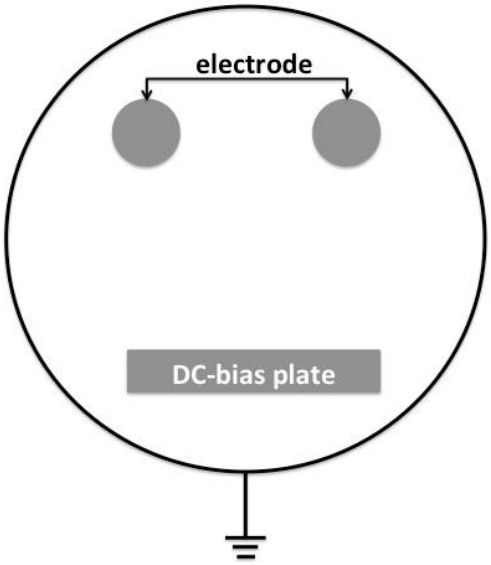

Figure 3. The schematic plasma modelling by using JMAG software.

3. RESULT AND DISCUSSION

3.1 The behaviour of electron density

The COMSOL software was employed to simulate the electron density behavior with variation of DC-bias and pressure. First, the pressure variation was simulated in the COMSOL software. The pressure was varied in the range of 30 to 80 Pa. The result of pressure variation is depicted in figure 4. The electron density increased from a low value of 1×10^{18} m^{-3} with increasing pressure to a high value of 3×10^{18} m^{-3}. Electron density is related to ionization process inside the chamber. At low pressure, fewer gas molecules were introduced to the chamber and less collisions occur. The ionization process occur from electron collision with the gas molecules. Ions and secondary electrons resulted in this process. Fewer gas molecules produced low

electron density. At high pressure, higher percentage of collision process occurred. As a consequence, a lot of electrons are produced through the ionization collision process and high electron density resulted.

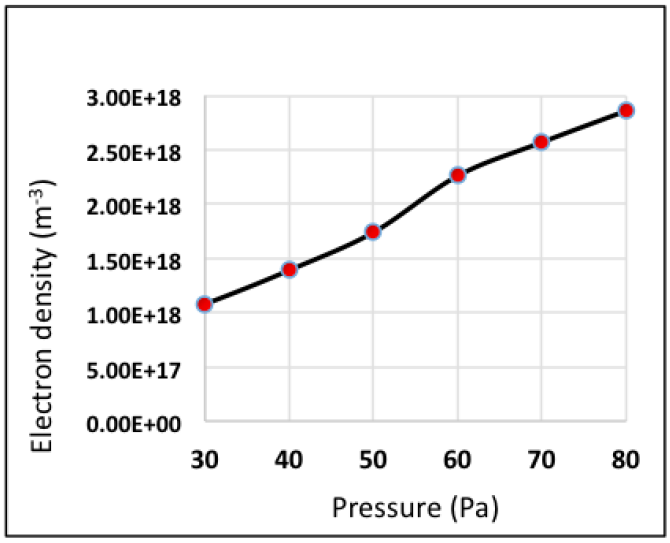

Figure 4. The effect of pressure variation in electron density

The DC-bias variation was also done in this simulation program. The effect of DC-bias variation is depicted in the figure 5. At low DC bias voltage, the electron density was 9.55×10^{17} m^{-3}. The electron density increased with the increasing of DC-bias voltage. In the simulation, the DC-bias voltage indicates the quantity of electrons inside the chamber. The high DC-bias accelerates the ionization process and increases the percentage of ionization process. As a result, high electron densities were produced in this condition

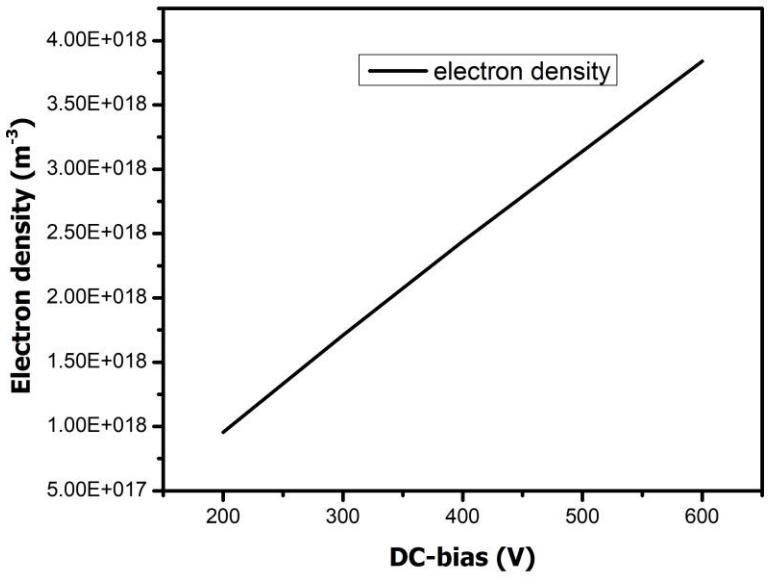

Figure 5. The effect of DC-bias variation in electron density

The result of the modelling program was compared with the measurement result from Langmuir probe in a previous study. The Langmuir probe was utilized to measure the electron density inside the chamber. The measurement result is shown in the figure 6. The Langmuir probe measurement result indicates the same trend with the simulation result. The pressure variation indicates high electron density was produced in higher pressure. The DC-bias variation showed the same result with the simulation result.

Basically, the DC-bias is utilized to accelerate the ion bombardment to the specimen in the experiment condition. In this case, the DC-bias increased the production of free electrons inside the chamber. The collisions of electrons and gas molecules also increased inside the chamber. As a result high electron density is produced in the high DC bias voltage. The simulation results are proposed to enhance the understanding of diagnosis by using measurement devices.

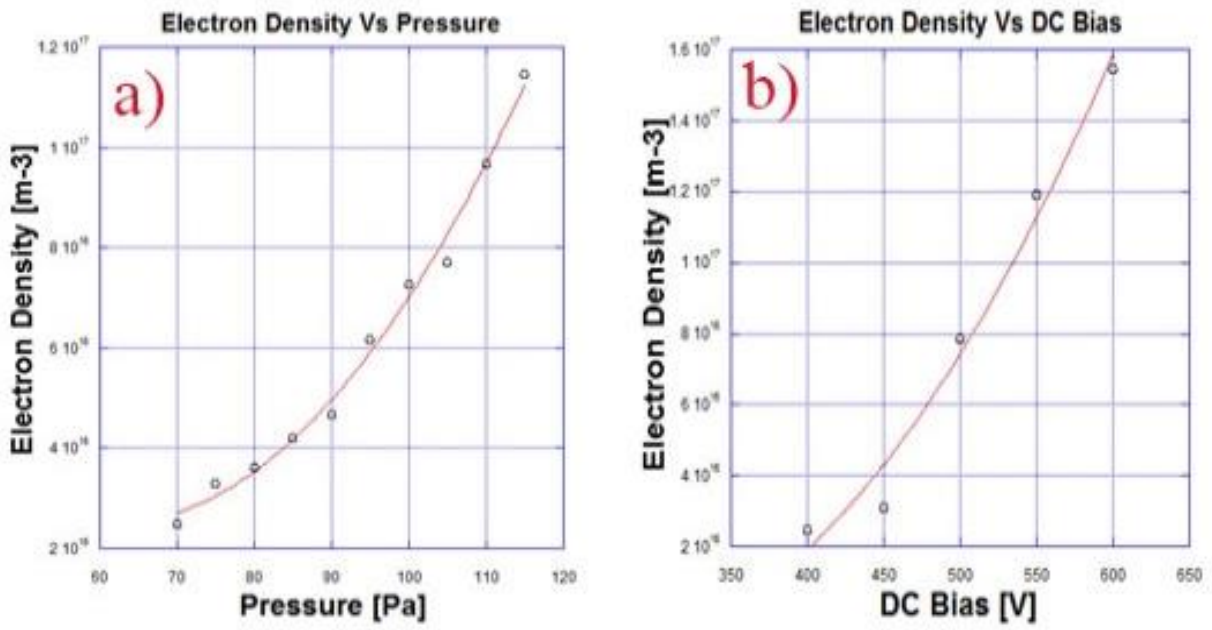

Figure 6. The pressure and DC bias variation results by using Langmuir probe

3.2 The effect of electric field distribution in the experiment set up

The JMAG software was employed to characterize the electric field distribution in the plasma system. The experiment set up has influence in the distribution of electric field. The voltage variations in the electrode and DC-bias have employed to characterize the electric field distribution. The results of electric field distribution in the present set up are shown in the figure 7. The green color indicates the main distribution of electric field in the simulation result.

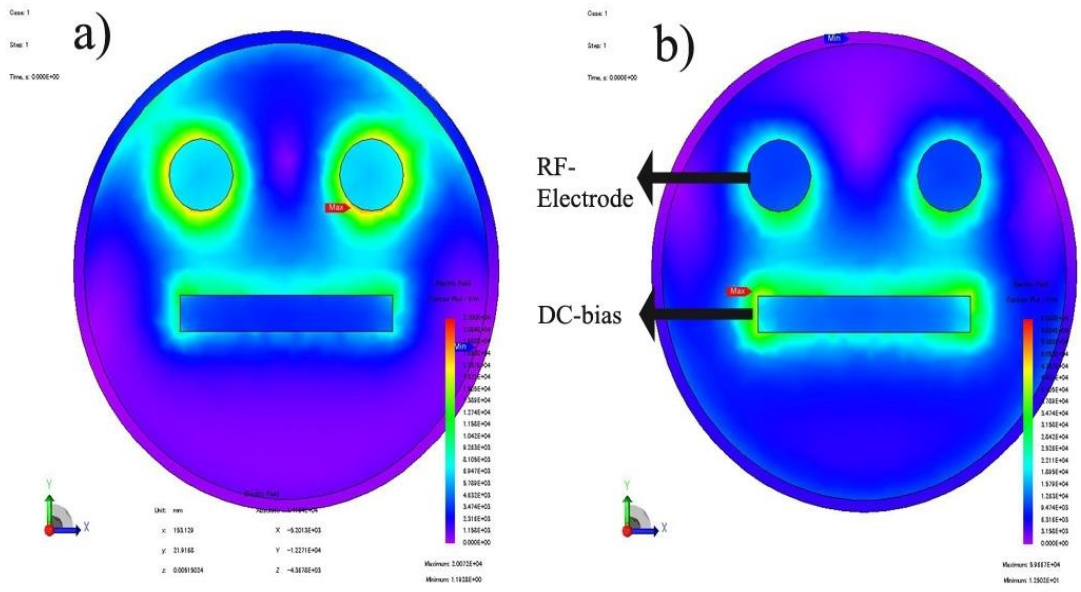

Figure 7. The electric field distribution in a) high RF voltage and low DC-bias voltage, b) low RF voltage and high DC bias voltage

Figure 7a represents the electrode at 250 V and the DC bias plate (-)100 V. The strong electric fields are concentrated in the electrode area. On the other hand, the DC-bias plate has weak concentrate of electric field. The main distribution of electric field is shown with the green color. However, the figure 7b represents a different electric field distribution result. The strong electric fields have shifted down to be close the sides of the DC bias plate due to the low voltage in the electrode and high voltage in the DC-bias plate. Both of the results have described the distribution of electric field in the present set up. The simulation result showed that the electric field direction depends on the high voltage which was applied in the electrode or DC-bias plate and is not uniformly distributed. In plasma processing the specimen are located on the DC-bias plate, modification of experiment set up has to be employed to solve this problem.

The new set up has been built to enhance the electric field distribution. The present set up has been modified by inserting a conductor as depicted in figure 8. This conductor is a hollow cathode, made from stainless steel. The hollow cathode is proposed to localize the glow discharge plasma and generate high electric field. The simulation result in figure 8a indicates a different distribution result from the previous result. The bright colour indicated in the area near the hollow cathode represents strong electric field. The bright colour almost covers the model of hollow cathode in the simulated result. This new diagnosis result has been applied in the present experiment in the laboratory as depicted in figure 8b. The glow discharge of hollow cathode plasma is concentrated inside the hollow tube area. The localized plasma is indicated with the strong and bright colour. The hollow cathode plasma provides high plasma density and effective for plasma etching (Yunata et al., 2016) and also plasma nitriding (Aizawa et al., 2017).

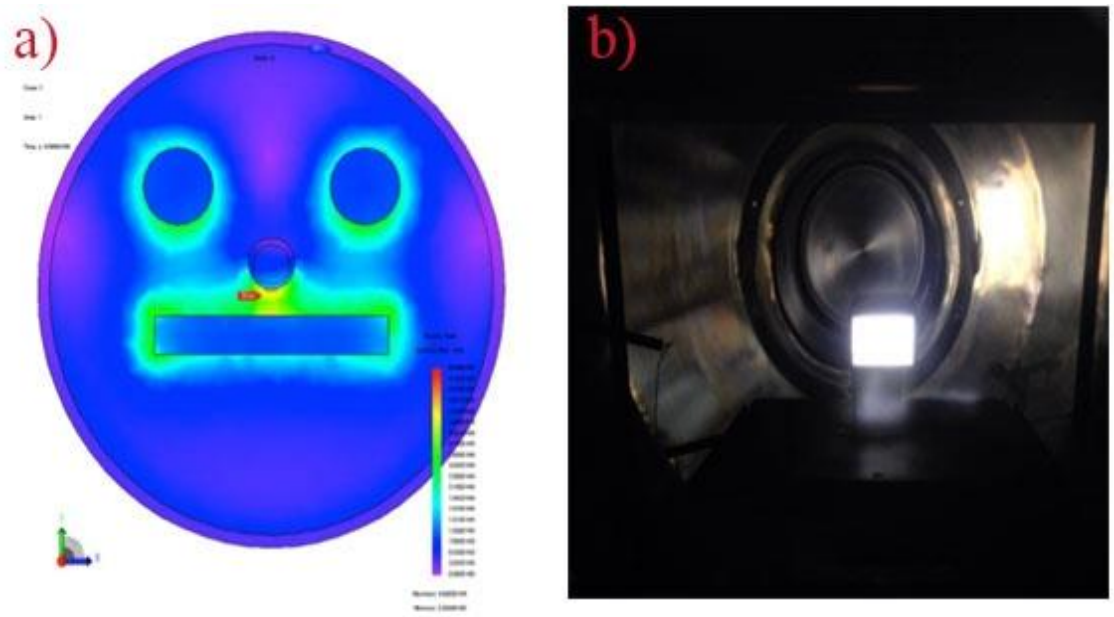

Figure 8. a) the electric field distribution in the new set up with hollow cathode, b) the glow discharge of hollow cathode plasma

4. CONCLUSION

The behaviour of electron density in the variation of DC-bias voltage and pressure was modelled with COMSOL software. The electron density increased with the increasing of DC-bias voltage and pressure. The high electron density indicated high percentage of ionization process inside the chamber. Electric field distribution was simulated using JMAG sofware. The simulation result showed the electric field distribution to be concentrated non-uniformly in the electrode or the DC-bias plate. A new set up with hollow cathode provided a solution to distribute the concentrated the electric field to cover over the surface of the DC-bias plate more evenly and in the centre between the hollow cathode and the DC-bias plate. High plasma density could be produced by using hollow cathode system.

5. ACKNOWLEDGEMENT

The authors would like to express their gratitude to Prof. Tatsuhiko Aizawa (Aizawa Sensei Laboratory) and Dr. Hijikata (Shibaura IT Japan) for their help in the experiment and modeling program.

6. REFERENCES

Aizawa T., et al.(2017). Fine piercing of electromagnetic steel sheets by plasma-nitrided tools, *Procedia Engineering* 247:1027-1032.

Brezmes A O., et al .(2014) Simulation of inductively coupled plasma with applied bias voltage using COMSOL, *Vacuum*. 109:52-60.

Dai X., et al.(2018). The emerging role of gas plasma in Oncotheraphy, *Biotechnology*. 36:1183-1198.

Fanelli F., et al.(2017). Atmospheric pressure non-equilibrium plasma jet technology: general features, specificities and applications in surface processing material, *Surface & Coatings Technology* 322 :174-201.

Kgoete F. M., et al.(2018) Study on properties and microstructure of Ti–Si–N coatings deposited in deep holes, *Jounal of Alloys and compounds* 769: 817-823.

Li C., et al.(2018). Optical emission spectroscopy study for pulsed frequency powered atmospheric He plasma. *Surface & Coating Technology* 353:316-323.

Mandal R., et al.(2018) Recent developments in cold plasma decontamination technology in the food industry, *Food Science & Technology* 80:93-103.

Meshcheryakova E., et al.(2015) Langmuir probe diagnostic of low-pressure inductively coupled argon plasma in magnetic field, *Physics Procedia* 71:121-126.

Misra N N., et al.(2019) In-package cold plasma technologies, *Journal of Food Engineering* 244:21-31.

Samal **S**., et al.(2017) Thermal plasma technology: The prospective future in material processing, *Journal of Cleaner Production* 142: 3131-3150.

Yunata E E., et al.(2013) Quantitative argon plasma characterization by Langmuir probe methode. The 7th SEATUC Symposium ITB Indonesia 1-5.

Yunata E E., et al.(2016) Micro-grooving into thick CVD diamond films via hollow-cathode oxygen plasma etching, *Manufacturing Letters* 8:16-20.

Zhao S., et al.(2017) Analysis of plasma oscillations by electrical detection in Nd:YAG laser welding, *Journal of Material Processing Tech* 249: 479–489.

EFFECT OF VARYING VOLTAGE ON ELECTRON DENSITY IN OXYGEN HOMOGENEOUS DIELECTRIC BARRIER DISCHARGE UNDER ATMOSPHERIC PRESSURE

Ali Akbar Khan[1a*], S L Yap[1b], Zaira Zaman Chowdhury[2c]

[1]Plasma Technology Research Centre, Department of Physics, Faculty of Science, University of Malaya, 50603, Kuala Lumpur, MALAYSIA. Email: aakhan.um.plasma@gmail.com[a]; yapsl@um.edu.my[b]
[2]Nanotechnology and Catalysis Research Centre (NANOCAT), University of Malaya, 50603, Kuala Lumpur, MALAYSIA. Zaira. Email: chowdhury76@gmail.com[c]
*Corresponding Author: aakhan.um.plasma@gmail.com
DOI: https://doi.org/10.22452/mjs.sp2019no3.2

ABSTRACT The formation of uniform dielectric barrier discharges (DBDs) under atmospheric pressure is a remarkable achievement with the addition of electronegative gasses in closed reactors. This work is the part of dielectric barrier discharge achieved under atmospheric pressure. A uniform glow discharge is produced in capacitive discharge reactor. An alternating voltage source (0-2.5) kV having frequency of 50Hz is applied across the two parallel disc electrodes. A couple of dielectrics (glass) used as a discharge barriers one on each electrode. The oxygen gas injected into the reactor controlled by mass flow controller with flow rate 30ml/min. The current-voltage waveforms for oxygen discharge achieved, fulfilling the basic conditions of discharge homogeneity. The diagnostic techniques rely on electrical discharge method and power balance method to differentiate discharges and estimate the electron density for different values of applied voltages. A significant relation is found indicating the variation of electron density with applied voltage.

Keywords: DBD, I-V waveforms, uniform discharge, power balance method, electron density

1. INTRODUCTION

Dielectric barrier discharge is typically produced when a dielectric material is inserted into the gap between the two conductive electrodes. DBDs are known to be produce for one or more dielectrics to sustain glow discharge without switching to arc discharge. The basic features of dielectric include the limitation of transmitted charge and to spread discharge over its surfaces. The addition of dielectric materials also bounds the discharge to produce only by alternating voltage sources. DBDs are distinguished from glow discharge in the sense that electrodes are not in physical contact with the plasma.

The generation and stabilization of dielectric barrier discharge has got much attention in the wake of primacy and its approach to industrial level. Uniform and stable discharges with vacuum reactor has many advantages in the fields of industry, medicine and environment, such as surface modification, deposition, cleaning, removal of pollution and sterilization (Fang et al., 2009; Mahendran & Alagusundaram, 2015; Rajasekaran et al., 2010; Zhi, Yuchang, & Hui, 2004). All of the above processes can be enhanced significantly by understanding the basic plasma manifestations and knowing its intrinsic parameters. The dielectric barrier discharge plasma is a synergical process depends upon a number of system parameters like electrodes gap, electrodes geometry, type of gas,

gas composition, applied voltage, type of dielectric material and source frequency etc. (Kanazawa, Kogoma, Moriwaki, & Okazaki, 1988; Okazaki, Kogoma, Uehara, & Kimura, 1993). According to the reported work by several investigators, the homogeneous mode of DBD is sustainable under reduced pressure (Ulrich Kogelschatz, 2003; Massines, Sarra-Bournet, Fanelli, Naudé, & Gherardi, 2012), While filamentary under atmospheric pressure (Massines et al., 1998). Although under atmospheric pressure the controlling of mean energy of electrons play a key role in approaching a homogeneous discharge. The mean energy of electron can be controlled by varying system parameters like shape of electrodes and type of dielectrics (U Kogelschatz, 2001). According to Kanazawa homogeneous discharge is closely related to the system parameters like geometry of the electrodes, the type of ignited gas and the source frequency. He achieved the homogeneous discharge in O_2/CF_4/He gasses under atmospheric pressure (Kanazawa et al., 1988; Okazaki et al., 1993; Tepper & Lindmayer, 2000). H. Ghomi investigated the effect of dielectric barrier and electrodes gap on the formation of homogeneous discharge (Ghomi, Safa, & Ghasemi, 2011). He used quartz plate and quartz plate plus paper separately as a dielectrics and achieved uniform discharge. He concluded from the experimental results that shorter electrodes gap, can stabilize the discharge more easily.

Non-thermal plasma with dielectric barrier discharges has many advantages related to their low cost, convenience and simplicity of the operating system (Eliasson & Kogelschatz, 1988; Ulrich Kogelschatz, Eliasson, & Egli, 1997). Under atmospheric pressure the use of expensive vacuum machines are no longer use, which justify the significance of DBDs (Di, Zhang, & Zhang, 2018; Niu et al., 2018). However the stabilization of discharge under atmospheric pressure is still a dilemma of ongoing research. Especially in electronegative gasses like air and oxygen. Because in these gasses the meta-stable species prevent ionization process and induce electron attachments reactions. So, these gasses generally induce filamentary discharges under atmospheric pressure (Nakagawa, Ono, & Oda, 2018; Shao, Wang, Zhang, & Yan, 2018).

Electron temperature and electron density are among the fundamental parameters of DBD plasma. Different diagnostic techniques are applied to measure the electron density and electron temperature. The diagnostic methods include optical emission spectroscopy (OES), electric probe, LASER Thomson Scattering and microwave interferometer (Goktas et al., 2007). Among these methods, electric probe and microwave based diagnostic techniques are not reliable under atmospheric pressure owing to the small volume of discharge between the electrodes and short pulse duration of plasma species. Also the reactive nature of oxygen plasma can harm the probe's tip and the recorded data becomes unreliable. Optical emission spectroscopy (OES) is the non-intrusive diagnostic technique which diagnose the plasma parameters like gas temperature, electron density (n_e) and electron velocity distribution function (EVDF). In OES technique the emitted photons are recorded in the form of intensity vs wavelength spectra. Line intensity ratio method is the type of OES technique utilized to calculate electron temperature and electron density of the reactive plasma (Balcon, Aanesland, & Boswell, 2007; Dong, Qi, Zhao, & Li, 2008). Power balance method is the other diagnostic technique to find the electron density in DBD plasma (Shrestha, Tyata, & Subedi, 2013). According to the power balance method the total power delivered to the plasma species is assumed to be balanced by the applied power.

In this study the parallel plate electrodes assembly is used to produce homogeneous discharge in oxygen gas under atmospheric pressure. The discharge initiated with frequency of 50Hz alternating voltage source. The homogenous discharge generated and spreads over the entire surfaces of dielectrics. The current-voltage waveforms recorded through digital oscilloscope (Tektronix TDS 2024B), showing full cycle of discharge current per half cycle of the applied voltage. Electron density is a significant parameter of stable discharge can be estimated using power balance method.

2. EXPERIMENTAL SET-UP

The dielectric barrier discharge schematic diagram is shown in figure. 1. The dielectric barrier discharge is obtained using specially designed reactor having fixed area of electrodes. The circular brass electrodes are put together in plane parallel configuration having diameter of 80mm and thickness of 6mm each. Each electrode is covered by a glass dielectric. The glass plate having diameter of 100mm with thickness of 3mm each. The electrodes assembly is fixed in triangular insulating stand to make it electrically isolate from reactor. The electrodes assembly is enclosed by a stainless steel reactor having internal diameter of 320mm (32cm) and height of 160mm (16cm). The discharge gap is set to 4mm between the electrodes. For homogeneous discharge, oxygen is supplied to the reactor with gas flow rate of 30ml/min controlled by mass flow controller (Model GFC-2104 via Flow Range 0~100 mL/min). An adjustable high voltage power source having amplitude from 0 to 2.5kV and frequency of 50Hz is connected to the upper electrode. The applied voltage between the electrodes is measured via a high voltage probe (Tektronix P6015A via 1000 x 3.0pF, 100 MΩ). The discharge current and transported charges can be measured by placing a resistor of 10kΩ and a capacitor (0.47µF) between the ground and bottom electrode respectively. The voltage and current waveforms are recorded in the personal computer, coupled with digital Oscilloscope (Tektronix TDS 2024B via 200MHz, 2GS/s). The applied frequency is fixed to 50Hz for all measurements, while applied voltage to the electrodes will be varying to study its effect on the electron density.

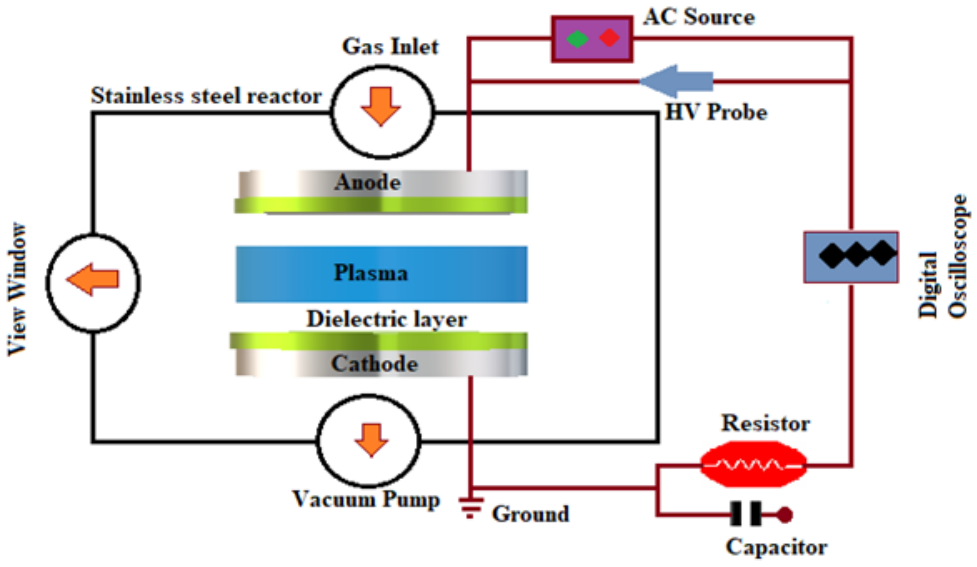

Figure 1. Schematic diagram of experimental set-up for DBD generation.

3. POWER BALANCE METHOD

Power balance characterization technique described by R. Shrestha determines electron density of DBD plasma operating at homogeneous mode (Shrestha et al., 2013; Subedi, Shrestha, Tyata, & Wong, 2017). According to this method the energy lost by each electron and ion within plasma can be written as;

$$E_{lost} = K.E_{ions} + K.E_{electrons} + K.E_{collisional} \quad (1)$$

Here $K.E_{ions}$ is the kinetic energy gained by ions falling down to plasma sheath wall (E_{ions}=$V_{pl} + 1/2T_e$), where V_{pl} is the plasma potential. $K.E_{electrons}$ be the mean kinetic energy lost per electron to the sheath wall having Maxwellian electron energy distribution ($E_{electrons} \approx 2\mathrm{K}T_e$). While $K.E_{collisional}$ is the collisional energy loss of electron-ion pairs produced (Guðmundsson). T_e is the electron temperature and its mean value is 3.6eV for oxygen DBD at atmospheric pressure (Hassouba, 2008).

Then the input power supplied and absorbed by the gas plasma is;

$$P_{abs} = \mathrm{IV} \quad (2)$$

Here "I" represents the discharge current and is given by;

$$\mathrm{I} = 2\mathrm{A}\mathrm{e}n_e V_b \quad (3)$$

Here "A" is the area of the electrodes, "e" is charge on electron, "n_e" is the electron density and"v_b" is the ion velocity entering into the sheath called Bohm velocity ($V_b = (\sqrt{eT_e/m_i}$). Where m_i is the mass of ion and T_e is the electron temperature.

And "V" is the potential difference between the two electrodes is calculated from potential gradient equation i.e.

$$\mathrm{V} = E_{lost}\mathrm{d} \quad (4)$$

Here "E" is the electric potential energy or kinetic energy of electrons between the electrodes and "d" is the separation between the electrodes. "E" will be lost in the case of kinetic energy and will be gain in the case of potential energy for electrons.

Inserting values in equation (1),

$$P_{\_abs} = 2Ae\ n_{\_e}\ v_{\_b}\ E_{\_lost}\ d \quad (5)$$

Then

$$n_{\_e} = P_{\_abs}/2Ae\ v_{\_b}\ E_{\_lost}\ d \quad (6)$$

Equation (6) will calculate the relative electron density for homogeneous mode of DBD. Here are the values mentioned in Table.1.

Table 1. List of system/plasma parameters and their calculated values.

S.N	System/Plasma parameters	Calculated values
1	Electrodes gap (d)	10mm (10^{-2}m)
2	Area of each electrode (A)	50.72 x 10^{-4}m^2
3	Bohm velocity (V_b)	4.64 x 10^3 m/s
4	Energy loss (E_{lost})	80.18eV
5	Charge on electron (e)	1.6 x 10^{-19}C
6	Power absorbed (P_{abs})	IV

4. RESULTS AND DISCUSSIONS

The homogeneous dielectric barrier in 4mm discharge gap obtained and corresponding oscillogrms of the applied voltage and discharge current are shown in Figures. 2-5. All measurements performed under atmospheric pressure. For homogeneous dielectric barrier discharge no filament is observed and discharge is radially symmetric between the electrodes covering the whole surfaces uniformly. The homogeneous discharge is relatively more luminous near the cathode surface. Also having single pulse of discharge current per half cycle of the applied voltage (All waveforms of figures. 2-5).

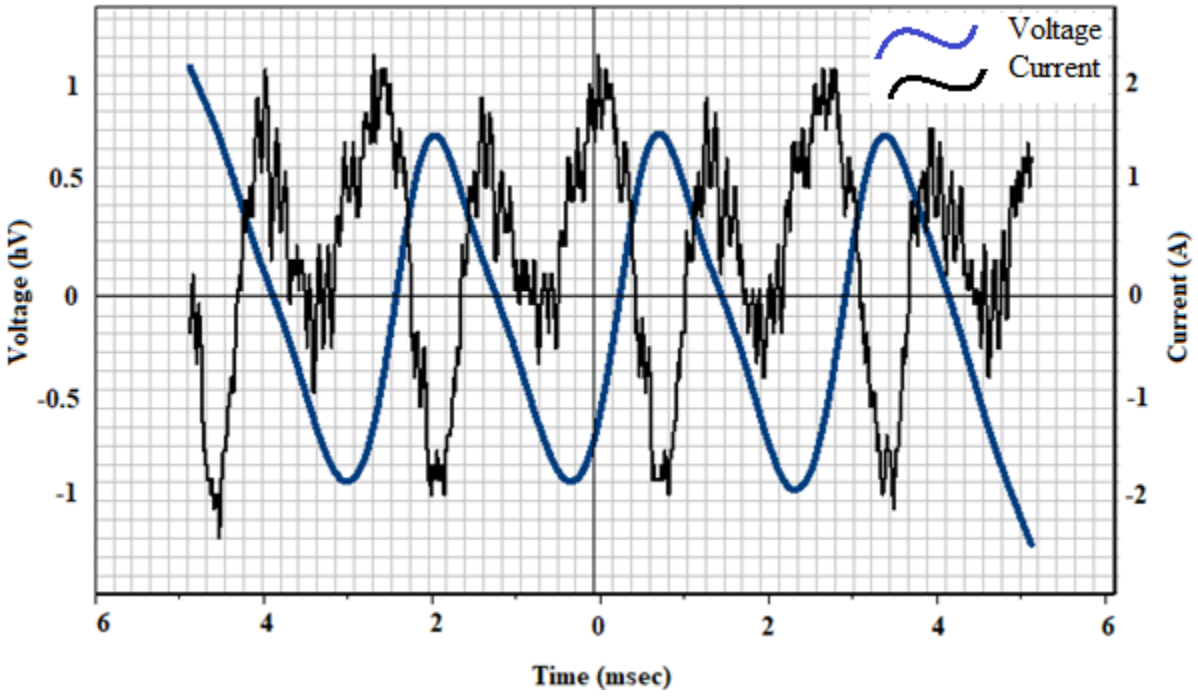

Figure 2. Current-voltage waveforms of the homogeneous discharge under applied voltage of 100V.

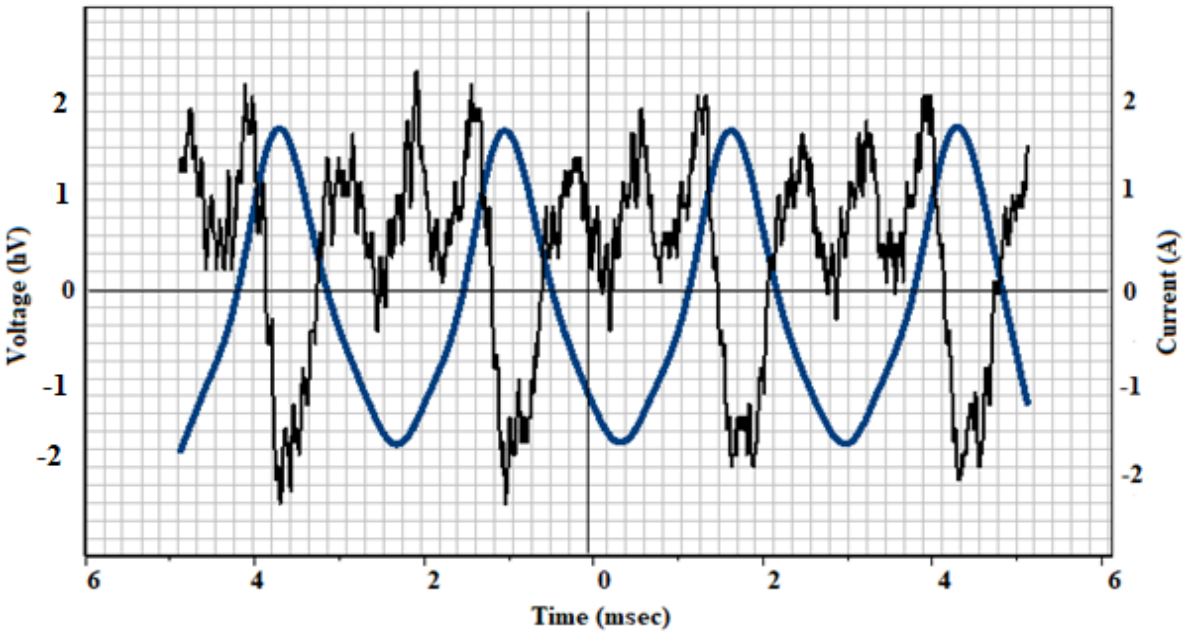

Figure 3. Current-voltage waveforms of the homogeneous discharge under applied voltage of 200V.

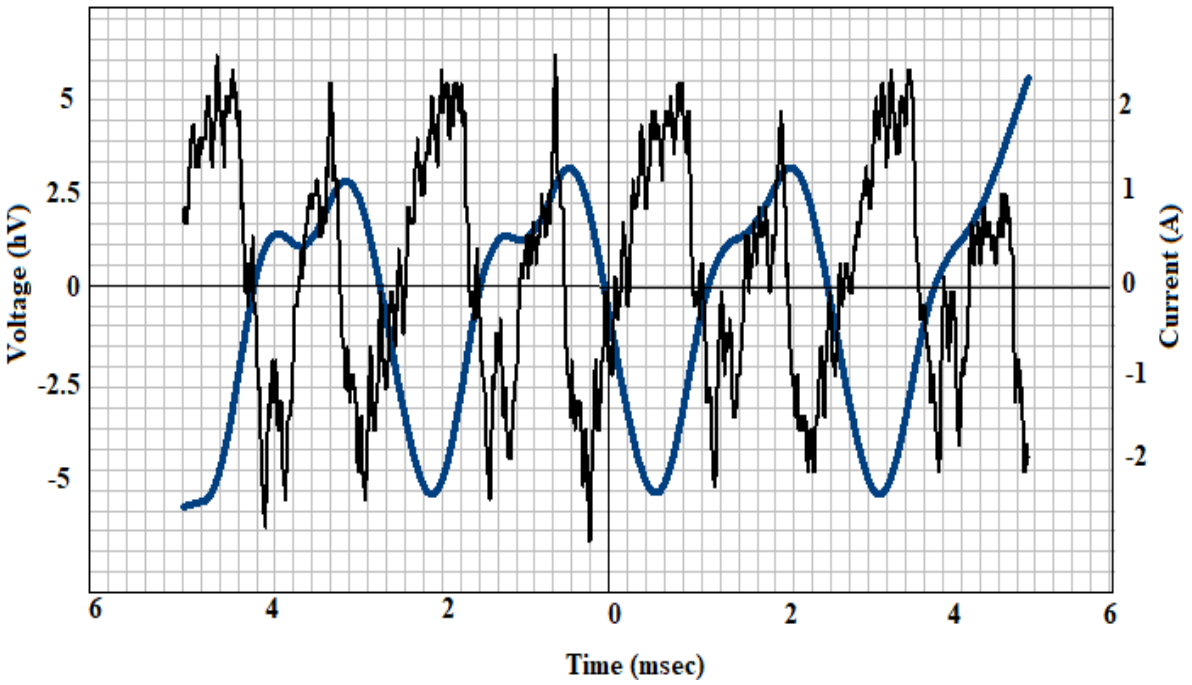

Figure 4. Current-voltage waveforms of the homogeneous discharge under applied voltage of 500V.

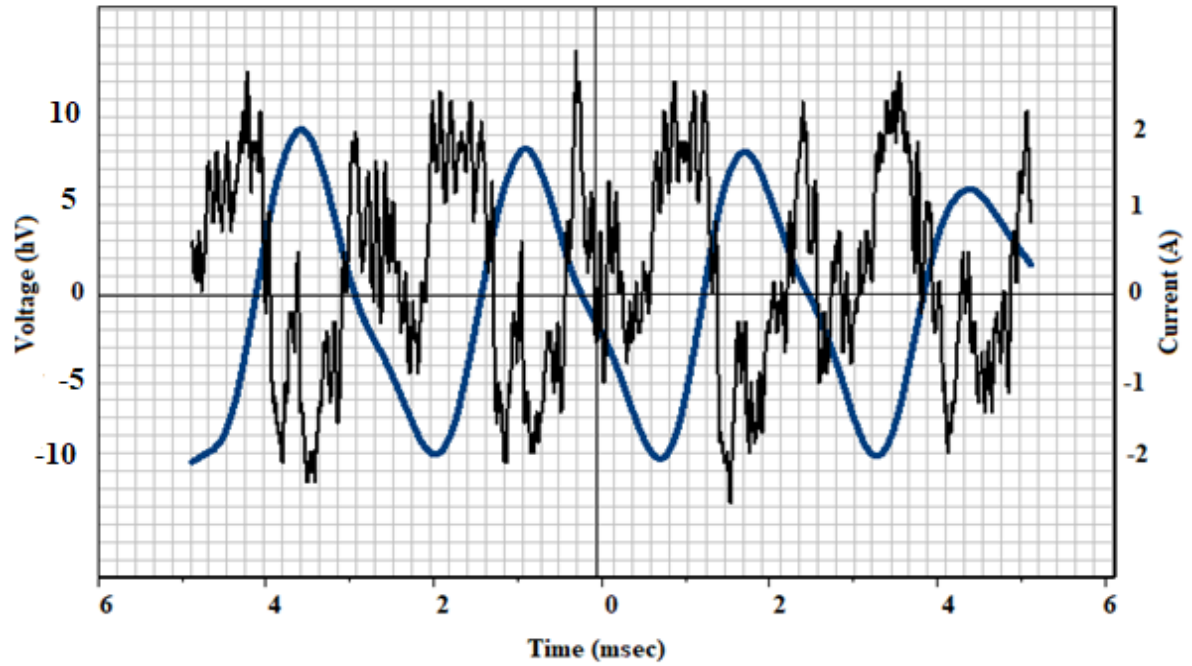

Figure 5. Current-voltage waveforms of the homogeneous discharge under applied voltage of 1kV.

The constant periods of both current and voltage waveforms should match each other for a perfect homogeneity. Since the polarity of AC voltage changes every half cycle, two luminous circles can be seen near the electrodes. The voltage current waveforms display sine wave,

representing the nature of discharge similar to glow discharge under reduced pressure. According to the voltage and current waveforms:

$$V = V_0 sin\omega t \quad (7)$$

$$I = I_0 \sin(\omega t + 90^0) \quad (8)$$

It is obvious from equation (8) that discharge current leads voltage by 90^0. In other words the discharge current is cosine with sinusoidal applied voltage. This shows the capacitive nature of DBD system. Sinusoidal voltage is an important parameter of discharge can change the electron density significantly. When the voltage is increased, the charge species will gain more and more energy from the applied electric field and its kinetic energy will increase. The increase in kinetic energy of the plasma species will change the collisional mode from elastic to inelastic. So, secondary electron emission process starts and will further enhance with the increase of applied voltage. The related I-V waveforms (2-5) show the confirmation of discharge homogeneity in oxygen discharge using different voltages under atmospheric pressure. The values of applied voltages and corresponding discharge currents are taken from waveforms (2-5) to estimate the electron density in each case using Eq. (6). The list of obtained values for electron densities with corresponding applied voltages are shown in Table 2.

Table 2. List of calculated values of electron density across each value of applied voltage.

S.N	Applied Voltage (V)	Electron density n_e x 10^{20} (m^{-3})
1	100	0.3
2	200	0.6
3	500	1.6
4	1000	3.3

The graph between the applied voltages and electron densities are plotted below. The voltage vs density graph shows that both quantities are directly related to each other. The graph depicts linear behavior for electron density as the applied voltage goes up.

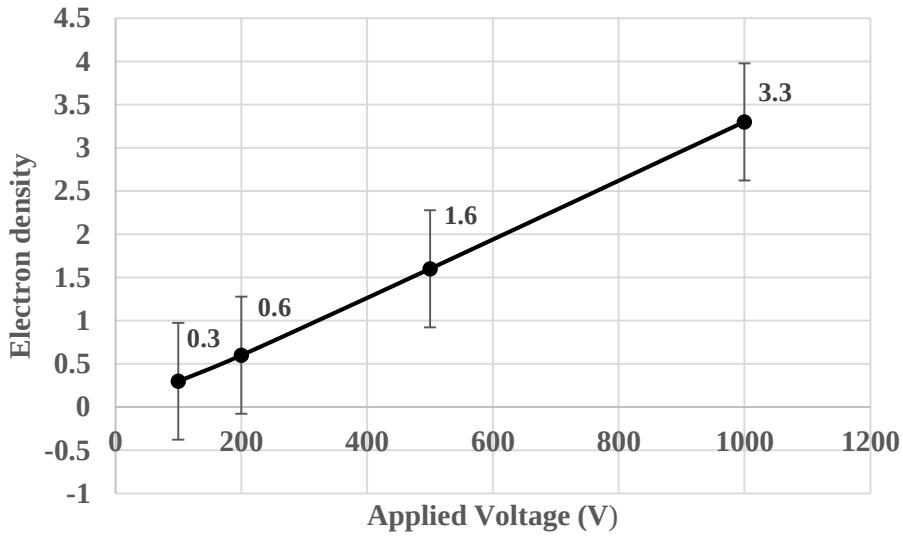

Figure 6. Graphical representation of variation between applied voltage and electron density.

5. CONCLUSIONS

It is demonstrated here that oxygen homogeneous discharge is produced using parallel plate disc electrodes system. Two glass plates are used as a dielectrics with 4mm electrodes gap. An alternating high power source (50Hz) employed to attain discharge. The discharge homogeneity conditions are verified by achieving current-voltage waveforms with the same periodicity. Electron density in homogenous discharge is highlighted here. The diagnostic technique relies on power balance method to estimate the value of electron density under atmospheric pressure. The results conclude that electron density and applied voltage are correlated by an important relation. The relation depicts that electron density increases with the increase of potential difference between the electrodes.

6. ACKNOWLEDGMENTS

The authors are thankful for the funding provided from the Grant No. RP044C-17AET and RP044D-17AET from the University of Malaya, Malaysia.

7. REFERENCES

Balcon, N., Aanesland, A., & Boswell, R. (2007). Pulsed RF discharges, glow and filamentary mode at atmospheric pressure in argon. Plasma Sources Science and Technology, 16(2), 217.

Di, L., Zhang, J., & Zhang, X. (2018). A review on the recent progress, challenges, and perspectives of atmospheric-pressure cold plasma for preparation of supported metal catalysts. Plasma Processes and Polymers, 15(5), 1700234.

Dong, L., Qi, Y., Zhao, Z., & Li, Y. (2008). Electron density of an individual microdischarge channel in patterns in a dielectric barrier discharge at atmospheric pressure. Plasma Sources Science and Technology, 17(1), 015015.

Eliasson, B., & Kogelschatz, U. (1988). UV excimer radiation from dielectric-barrier

discharges. Applied Physics B, 46(4), 299-303.

Fang, Z., Xie, X., Li, J., Yang, H., Qiu, Y., & Kuffel, E. (2009). Comparison of surface modification of polypropylene film by filamentary DBD at atmospheric pressure and homogeneous DBD at medium pressure in air. Journal of Physics D: Applied Physics, 42(8), 085204.

Ghomi, H., Safa, N. N., & Ghasemi, S. (2011). Investigation on a DBD plasma reactor. IEEE Transactions on plasma science, 39(11), 2104-2105.

Goktas, H., Demir, A., Kacar, E., Hegazy, H., Turan, R., Oke, G., & Seyhan, A. (2007). Spectroscopic measurements of electron temperature and electron density in electron beam plasma generator based on collisional radiative model. Spectroscopy letters, 40(1), 183-192.

Guðmundsson, J. T. Notes on the electron excitation rate coefficients for argon and oxygen discharge: Raunvísindastofnun Háskólans.

Hassouba, M. A. (2008). Determination of the electrons temperature in a dielectric barrier discharge. Plasma Devices and Operations, 16(2), 81-88.

Kanazawa, S., Kogoma, M., Moriwaki, T., & Okazaki, S. (1988). Stable glow plasma at atmospheric pressure. Journal of Physics D: Applied Physics, 21(5), 838.

Kogelschatz, U. (2001). Filamentary and diffuse barrier discharges. Paper presented at the 2001 APP Spring Meeting Bad Honnef.

Kogelschatz, U. (2003). Dielectric-barrier discharges: their history, discharge physics, and industrial applications. Plasma chemistry and plasma processing, 23(1), 1-46.

Kogelschatz, U., Eliasson, B., & Egli, W. (1997). Dielectric-barrier discharges. Principle and applications. Le Journal de Physique IV, 7(C4), C4-47-C44-66.

Mahendran, R., & Alagusundaram, K. (2015). Uniform discharge characteristics of non-thermal plasma for superficial decontamination of bread slices. International Journal of Agricultural Science and Research (IJASR), 5(2), 209-212.

Massines, F., Rabehi, A., Decomps, P., Gadri, R. B., Ségur, P., & Mayoux, C. (1998). Experimental and theoretical study of a glow discharge at atmospheric pressure controlled by dielectric barrier. Journal of Applied Physics, 83(6), 2950-2957.

Massines, F., Sarra-Bournet, C., Fanelli, F., Naudé, N., & Gherardi, N. (2012). Atmospheric pressure low temperature direct plasma technology: status and challenges for thin film deposition. Plasma Processes and Polymers, 9(11-12), 1041-1073.

Nakagawa, Y., Ono, R., & Oda, T. (2018). Effect of discharge polarity on OH density and temperature in coaxial-cylinder barrier discharge under atmospheric pressure humid air. Japanese journal of applied physics, 57(9), 096103.

Niu, C.-B., Qin, S., Zhang, X., Zhao, H.-X., Liu, X., Mu, H.-B., & Zhang, G.-J. (2018). Discharge characteristics of argon atmosphere dielectric barrier with different pd values. Paper presented at the 2018 12th International Conference on the Properties and Applications of Dielectric Materials (ICPADM).

Okazaki, S., Kogoma, M., Uehara, M., & Kimura, Y. (1993). Appearance of stable glow discharge in air, argon, oxygen and nitrogen at atmospheric pressure using a

50 Hz source. Journal of Physics D: Applied Physics, 26(5), 889.

Rajasekaran, P., Mertmann, P., Bibinov, N., Wandke, D., Viöl, W., & Awakowicz, P. (2010). Filamentary and homogeneous modes of dielectric barrier discharge (DBD) in air: investigation through plasma characterization and simulation of surface irradiation. Plasma Processes and Polymers, 7(8), 665-675.

Shao, T., Wang, R., Zhang, C., & Yan, P. (2018). Atmospheric-pressure pulsed discharges and plasmas: mechanism, characteristics and applications. High voltage, 3(1), 14-20.

Shrestha, R., Tyata, R., & Subedi, D. (2013). Effect of applied voltage in electron density of homogeneous dielectric barrier discharge at atmospherice pressure. Himalayan Physics, 4, 10-13.

Subedi, D. P., Shrestha, R., Tyata, R. B., & Wong, C. S. (2017). Generation and diagnostics of atmospheric pressure dielectric barrier discharge in argon/air. Indian Journal of Pure & Applied Physics (IJPAP), 55(2), 155-162.

Tepper, J., & Lindmayer, M. (2000). Investigations on two different kinds of homogeneous barrier discharges at atmospheric pressure. Paper presented at the Proc. of Int. Symp. on High Pressure, Low Temperature Plasma Chemistry.

Zhi, F., Yuchang, Q., & Hui, W. (2004). Surface treatment of polyethylene terephthalate film using atmospheric pressure glow discharge in air. Plasma Science and Technology, 6(6), 2576.

ANTIOXIDANT ACTIVITIES OF CURCUMIN TO MDA BLOOD SERUM CONCENTRATION AND LEAD LEVELS IN LIVER OF MICE

Sugiharto[1a*], Win Darmanto[1b], Sri Puji Astuti Wahyuningsih[1c], Alfiah Hayati[1d], Yani Martha[1e], Putri Olivia[1f], Kevita Putri[1g]

[1]Biology Department, Faculty of Science and Technology, Universitas Airlangga, Surabaya–60115, INDONESIA.
Email: totoksbioua@gmail.com[a]; windarmanto@fst.unair.ac.id[b]; sri-p-a-w@fst.unair.ac.id[c]; alfiahayati64@yahoo.com[d]; Yani.martha@yahoo.co.id[e]; Putri.oliviar@gmail.com[f]; kevita.putri@gmail.com[g]
[*]Corresponding author: totoksbioua@gmail.com ; sugiharto@fst.unair.ac.id
Submitted: 22nd December 2018 Accepted: 9th July 2019 Published: 30th November 2019
DOI: https://doi.org/10.22452/mjs.sp2019no3.3

ABSTRACT Human and animals can accidentally be exposed to heavy metals from the environment such as lead (Pb). Lead may induce oxidative stress. It can increase the production of free radicals, and induces several responses in physiological and biochemical functions of the body. Curcumin, a major component of turmeric, is commonly used as a spice and in traditional medicine. The objective of this research was to evaluate the antioxidant activities of curcumin in mice that were exposed to lead. Research was conducted using twenty five male mice, which were grouped into five treatments: P1 (control), P2 (Pb 75 mg/kg BW), P3 (Pb 150 mg/kg BW), P4 (Pb 75 mg/kg BW + curcumin 20 ppm), P5 (Pb 150 mg/kg BW + curcumin 20 ppm). The results showed that antioxidant activities of curcumin was very strong with an IC-50 was 9.0 ppm. Pb exposure increased MDA level (17.143–17.891 μM) and Pb level in the liver (0.070–0.071 mg/kg BW). Administration of curcumin 20 ppm have the potential to reduced MDA level (14.592–15.714 μM) and reduce Pb levels (0.035–0.038 mg/kg BW).

Keywords: Antioxidant, Curcumin, Lead, Liver, MDA

1. INTRODUCTION

One of the heavy metals accumulation that has the potential to poison is lead (Pb). The main mechanism of lead toxicity is *via* oxidative stress induction. It induces several responses to physiological and biochemical functions in the body. The indicators of the occurrence of heavy metal poisoning in tissues are blood components and liver function. Lead toxicity depends on the dose and time length of exposure (Flora et al., 2012; Fuente et al., 2002; Xu et al., 2008).

Sharma and Singh (2014) showed that the administration of lead-acetate in mice at 150 mg/kg BW for 40 days, significantly reduced the endogenous antioxidant enzyme, superoxide dismutase (SOD) and catalase (CAT) and increased lipid peroxidation in kidney organs, and inactivated glutathione (GSH) and antioxidant enzymes such as SOD and CAT (Flora et al., 2012). According to Al-Fartosy et al., (2017), exposure of petroleum pollutants and heavy metals increases malondialdehyde (MDA) levels in gasoline station workers through induction of oxidative stress reactive oxygen species (ROS) are produced continuously. The endogenous antioxidant enzymes help to neutralize the impact of ROS. Hayati et al.,

(2017) observed that heavy metals in the gonads and the liver of *Barbodes sp* resulted in cell damage and cell necrosis. Lead exposure at doses of 50 mg/Kg and 100 mg/kg BW causes oxidative stress and alter protein expression associated with apoptosis in liver of mice (Xu et al., 2008).

Oxidative stress can be alleviated with exogenous antioxidants. Antioxidant stops the oxidation process by neutralizing free radicals that formed during oxidation and convert free radicals into stable forms. The function of antioxidants is to eliminate ROS generated in the body. Indonesia is a mega biodiversity country, with plants possesing medicinal properties such as curcumin, a main constituent of tumeric rhizomes. Sugiharto et al., (2013) and Sugiharto et al., (2016) reported that curcumin has been shown to exhibit strong antioxidant activities with low toxicity, and as a tyrosinase inhibitor to reduce hyperpigmentation in cell B16-F1, because it have phenolic compounds that are responsible for its antioxidant activities (Priyadarsini et al., 2003). The aim of this research was to investigate the antioxidant activities of curcumin in mice exposed to lead. The antioxidant activities of curcumin were evaluated by 2,2-diphenyl-1-picrylhydrazyl (DPPH) method, and its effects studied from concentration of blood serum MDA and lead level in the liver of mice.

2. MATERIAL AND METHODS

2.1 Animals and Materials

The research used male mice (*Mus musculus*, strains Balb/C), aged 8-10 weeks from the Faculty of Pharmacy, Airlangga University, Surabaya. Curcumin (Sigma-Aldrich C1386), DPPH (Sigma-Aldrich D9132), MDA kit Bioassay TBARS Assay Kit (DTBA-100), lead acetate was obtained from local chemical stores. Atomic Absorption Spectroscopy (AAS – Perkin Elmer Analyst 300), Eppendorf micropipette, centrifuge (Eppendorf 5424R), microplate reader (Multiskan Go – Thermo scientific), was carried out in Molecular Genetic Laboratory, Faculty of Sciences and Technology, Airlangga University, Surabaya.

The use of animal subjects for the research have been approved by Ethics Committee of the Faculty of Veterinary Medicine, Airlangga University (certificate no. 2.KE.100.06.2018).

2.2 Determination of Curcumin Antioxidant Activity

The antioxidant activity of curcumin was determined by DPPH methods (Lee et al., 2009). Radical scavenging activities were tested using 100 µl curcumin at various concentrations placed into 96 well plates with ethanol solution as a control. Five microliter 2.5 mM DPPH was added followed by 30 minutes incubation in the dark. Antioxidant activity of vitamin C was compared to curcumin. The percentage of scavenging activity measured at $\lambda = 517$ nm in a microplate reader was calculated by equation (1):

$$\% \text{ Scavenging Activity} = [(\text{Abs. control} - \text{Abs. sample}) / \text{Abs. control}] \times 100 \% \quad (1)$$

2.3 Lead Exposure and Curcumin Treatment

Twenty five mice were acclimated for seven days and then randomly gathered into five treatment groups normalized to per kg body weight (BW):

P1: 0.4 mL of distilled water (control)

P2: 0.4 mL of lead solution 75 mg/kg BW
P3: 0.4 mL of lead solution 150 mg/kg BW
P4: 0.4 mL of lead solution 75 mg/kg BW + 0.4 mL curcumin 20 ppm
P5: 0.4 mL of lead solution 150 mg/kg BW + 0.4 mL curcumin 20 ppm

The lead treatment was given every morning (08:00 to 09:00 hours), while curcumin was administered in the afternoon (15:00 to 16:00 hours). The treatments were administered orally for 30 days using injection syringe with a round tip (a cannula).

On the last day of treatment, the mice were sacrificed, and blood samples were taken using intra-cardiac technique. The blood samples were centrifuged at 3,000 rpm for 10 minutes at 10 °C by centrifuge to harvest the serum. Liver tissues were also taken for determining lead level by AAS (Ugya and Imam, 2017) and histopathological analysis by Hematoxylin Eosin (HE) staining (Sugiharto et al., 2018).

2.4 MDA Assay

The assay was performed using Bioassay TBARS Assay Kit (DTBA-100) according to the kit manufacturer instruction (BioAssay System). Briefly, 100 µL of serum sample and 200 µL of 10 % TCA were mixed in a microtube, and incubated on ice for five minutes. The mixture was centrifuged at 14,000 rpm for 5 minutes. Then, 200 µL of the supernatant was transferred into a fresh tube. Standard MDA, serum sample and 200 µL TBA reagent were mixed through vortexing, then incubated at 100 °C for 60 min. After the tubes were cooled to room temperature, they were re-centrifuged after vortexing. Aliqouts of 100 µL mixture were loaded into 96 well plates, and absorbance (*Abs*) measured at $\lambda = 535$ nm on a microplate reader. MDA level was calculated using equation (2):

$$\text{MDA level } (\mu M) = \{(Abs_{\text{sample}} - Abs_{\text{blank}})/\text{Slope standard MDA}\} \times \text{dilution factor} \quad (2)$$

2.5 Determination of Lead Concentration in Liver

Lead level analysis was performed with slight modification from Ugya and Imam (2017), by drying the liver in 180 °C oven. Sample was mashed and weighed approximately two grams. Approximately 20 ml of HNO_3 was added and heated at 300 °C until brown-colored fumes disappeared. Perchlorate nitrate was added to the mixture in a ratio of 1:1 (*v/v*), followed by heating to obtain a clear solution. The mixture was chilled and then transferred into 100 ml flask for filtration using Whatman no. 41 filter paper. The filtrate was used for Atomic Absorption Spectroscopy (AAS) measurement.

2.6 Statistical Analysis

The statistical analyses were performed using SPSS 16.0. ANOVA and Duncan's Multiple Range Test (DMRT) at 5 % significance level were applied. Data for antioxidant activity of curcumin was fitted to a logarithmic model to determine IC_{50}.

3. RESULTS AND DISCUSSION

3.1 Antioxidant Activity of Curcumin

Antioxidants stop the oxidation process by neutralizing free radicals and convert them into stable forms. The strength

of an antioxidant activity is inferred from its IC_{50} value *viz.* the smaller its value, more powerful its activity. The widely used method to measure antioxidant activity is DPPH assay, which is easy, fast and sensitive. DPPH is a stable free radical that can react with antioxidant compounds through H atoms donation. The reaction changes the color of DPPH solution and its absorbance can be determined at 517 nm (Molyneux, 2004).

In this research, the IC_{50} of curcumin was determined at 9.0 ppm relative to vitamin C (3.0 ppm) (Figure 1). A compound is a very potent antioxidant if its IC_{50} < 50 ppm. It is clear that the antioxidant activities of curcumin and vitamin C are similarly strong. Curcumin acts as an antioxidant because it contains phenolic compounds, and the associated and donatable H atoms are responsible for the antioxidant activities (Molyneux, 2004; Nimse and Pal, 2015; Priyadarsini et al., 2003).

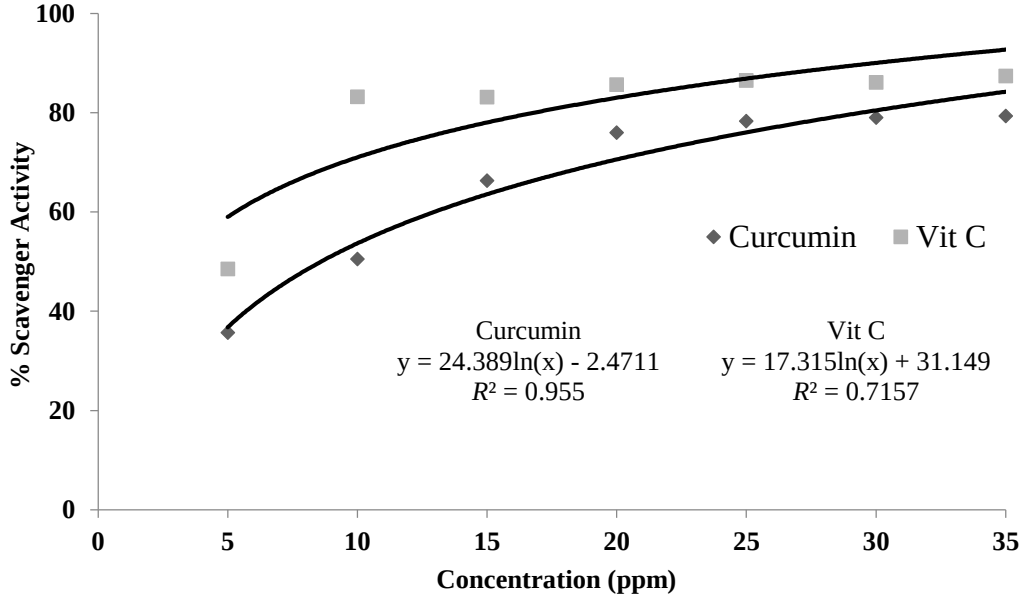

Figure 1. The logarithmic trendline antioxidant activity of curcumin and vitamin C

3.2 Assay of MDA Concentration

Lead exposure induces several physiological and biochemical responses in the cells. According to Flora et al. (2012), the main mechanism of lead toxicity is *via* oxidative stress. It leads to the increase in free radicals production and reduced endogenous antioxidants.

Lead exposure can increase concentration of mice blood serum MDA, and curcumin administration helped to reduce the MDA levels (Table 1). On the contrary, ANOVA test had shown an insignificant results (*p=0.067*). Al-Fartosy et al., (2017), reported that exposure of petroleum pollutants and heavy metals increased MDA levels in gasoline station workers. Lead acetate significantly increased the levels of ROS and MDA in mice (Xu et al., 2008). Acute and chronic

lead exposure increased renal lipid hydroperoxides, and decreased SOD and CAT as antioxidant enzymes (Sharma and Singh, 2014). Lead exposure also decreased both of SOD enzyme in the blood serum and liver cell (Sugiharto et al., 2018). The degenerative effect in liver cells is due to the production of ROS following lead-induced oxidative stress that may eventually result in cell death.

The reduction in the presence of endogenous antioxidant enzymes, which is supposedly to neutralize the impact of ROS, necessitates the intake of exogenous antioxidants. The administration of curcumin can help in reducing blood serum MDA concentration since it is a powerful antioxidant (Sugiharto et al., 2018).

Table 1. Concentration of MDA in blood serum (µM)

Treatments	Replication						Conc. of MDA ± SD (µM)
	1	2	3	4	5	6	
Control	10.408	11.837	14.490	16.735	15.510	13.265	13.707 ± 2.350
Pb 75	13.878	12.857	16.327	17.347	23.265	23.673	17.891 ± 4.615
Pb 150	15.510	15.918	17.551	17.347	18.776	17.755	17.143 ± 1.218
Pb 75 + Cur	16.327	16.531	14.898	13.878	14.694	17.959	15.714 ± 1.494
Pb 150 + Cur	16.531	17.755	14.898	14.286	11.837	12.245	14.592 ± 2.326

3.3 Determination of Lead Concentration in Liver

Elevated level of lead was determined in liver samples of mice treated with lead solution, and administration of curcumin seemed to reduce it (Table 2). There are several studies that have reported that higher level of lead in organs. Amriani et al., (2011) observed that there was an increase in lead and zinc levels in shells of *Anadara granosa* and *Polymesoda bengalensis* from heavy metals-contaminated Kendari Bay. Faix et al., (2005) observed that the concentration of lead was significantly higher in the rumen, colon, liver and kidneys in the sheep that have been long-term high heavy metal intake. The impact of lead pollution was also observed in vegetables (Fauziah et al., 2011; Ugya and Imam, 2017).

Table 2. Concentration of lead in the liver (mg/kg)

Treatments	Replication		Conc. of Lead ± SD (mg/kg)
	1	2	
Control	0.023	0.028	0.026 ± 0.004
Pb 75	0.073	0.068	0.071 ± 0.004
Pb 150	0.075	0.064	0.070 ± 0.008
Pb 75 + Cur	0.032	0.037	0.035 ± 0.004
Pb 150 + Cur	0.036	0.040	0.038 ± 0.003

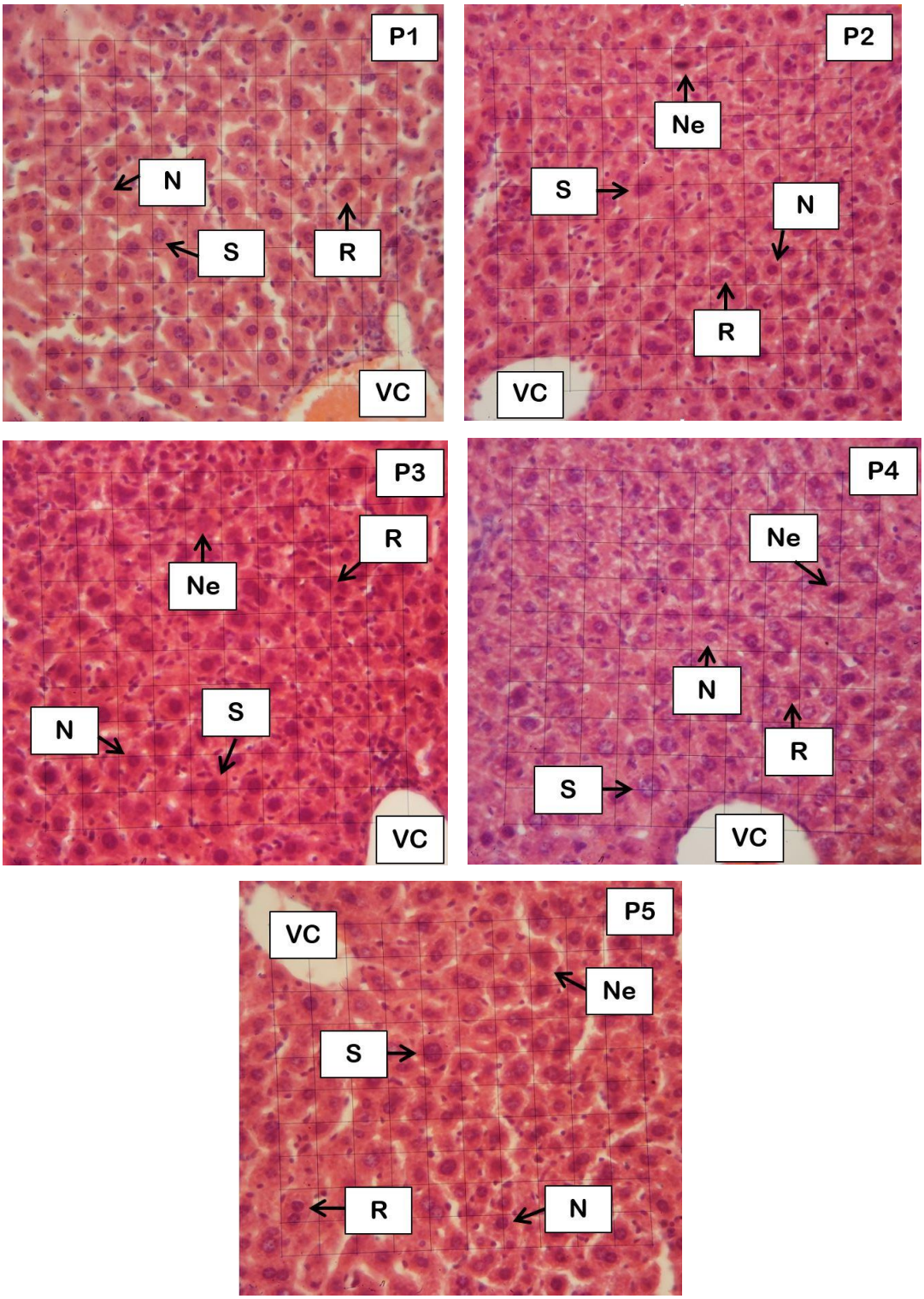

Figure 2. Hepatocyte cells, N = normal; S = swollen; R = regeneration; Ne = necrosis; VC = vena centralis. P1 = Control; P2 = Pb75; P3 = Pb150; P4 = Pb75+Cur; P5 = Pb150+Cur (Magnification 400 ×)

Table 3. The histopathology of hepatocyte cells

Treatment	% Hepatocyte cells			
	Normal	**Necrosis**	**Swollen**	**Regeneration**
Control	70.96 ± 5.40 [a]	9.33 ± 4.51 [a]	7.59 ± 2.00 [a]	12.11 ± 2.06 [a]
Pb 75	37.01 ± 3.09 [c]	29.99 ± 4.90 [c]	17.36 ± 1.02 [cd]	15.63 ± 5.41 [a]
Pb 150	41.40 ± 4.22 [c]	27.33 ± 7.32 [c]	16.11 ± 6.86 [bc]	13.00 ± 1.00 [a]
Pb 75 + Cur	36.85 ± 1.53 [c]	30.24 ± 1.42 [c]	21.54 ± 1.90 [d]	11.37 ± 1.73 [a]
Pb 150 + Cur	52.08 ± 5.95 [b]	20.76 ± 2.58 [b]	12.54 ± 1.42 [b]	14.62 ± 2.94 [a]

The different letters show significant differences in the Duncan's test ($p < 0.05$)

Liver histopathology showed that lead exposure increased the number of necrotic cells and the swollen cells, concomitantly decreasing the normal cells (Figure 2, Table 3). Lead may induce oxidative stress and change the expressions of apoptosis-related proteins in mouse liver (Xu et al., 2008). Hayati et al., (2017) observed that heavy metals in the liver of Barbodes sp. can cause cell damage and necrosis cells. Exposure to lead and aluminum may increase the risk of congenital heart disease (CHD) occurrence, and may lead to a decline in the activity of antioxidant enzymes (Liu et al., 2018).

Sugiharto et al., (2018) observed that curcumin as an antioxidant can restore the damaged cells. The potential protective effects of curcumin mainly attributed to its antioxidant properties against heavy metals intoxication. Curcumin has strong antioxidant property by acting as ROS scavengers, hydrogen donors, increasing the SOD activity, reducing MDA levels (Molyneux, 2004; Shah and Jain, 2016). The 1, 3-diketone moiety of curcumin can readily chelate heavy metal ions (Raj and Shankaran, 2016). It's also relate to high tendency of chelating heavy metals. Curcumin prevents structural damage and increases antioxidant enzymes to protecting hepatic cells from oxidative damage (Khan et al., 2019).

4. CONCLUSION

Curcumin exhibited strong antioxidant activity with IC50 9.0 ppm. Lead exposure increased MDA and Pb levels in the liver. Administration of curcumin at 20 ppm have the potential to reduced MDA level and Pb level/kg BW.

5. ACKNOWLEDGMENTS

We would like to thank to Faculty Sciences and Technology, Universitas Airlangga, for research grant No.1915/UN3.1.8/LT/2018.

6. REFERENCES

Al-Fartosy A.J.M., Shanan S.K., and Awad N.A., (2017). Biochemical Study of The Effects of Some Heavy Metals on Oxidant Antioxidant Status in Gasoline Station Workers Basra-Iraq, International Journal of Scientific and Research Publications, 7(2): 83-94.

Amriani, Hendrarto B., and Hadiyarto A., (2011). Bioakumulasi Logam Berat

Timbal (Pb) Dan Seng (Zn) Pada Kerang Darah (Anadara granosa L.) Dan Kerang Bakau (Polymesoda bengalensis L.) Di Perairan Teluk Kendari, Jurnal Ilmu Lingkungan 9(2): 45-50.

Faix S., Z. Faixova Z., Boldizarova K., and Javorsky P., (2005). The Effect of Long-Term High Heavy Metal Intake on Lipid Peroxidation of Gastrointestinal Tissue in Sheep, Veterinárni Medicina – Czech 50(9): 401–405.

Fauziah S.H., NurHajar W.S., and Agamuthu P., (2011). Heavy Metal Accumulation in Ipomoea reptans and Helianthus annuus, Malaysian Journal of Science 30(1): 36-44.

Flora G., Gupta D., and Tiwari A., (2012). Toxicity of Lead: A Review With Recent Updates, Interdisciplinary Toxicology 5(2): 47-58.

Fuente H.D., Perez D.P., Baranda L., Barriga F.D., Alanis V.S, Layseca E., and Amaro R.G., (2002). Effect of Arsenic, Cadmium, and Lead on The Induction Apoptosis of Normal Human Mononuclear Cells, Clinical & Experimental Immunology 129: 69-77.

Hayati A., Sugiharto, Abdizen M., Solikha B.M., Maulidyah N., Tiantono N., Seta A.R., Widyana H., Restinastiti I., Ziky D., and Winarni D., (2017). Bioaccumulation of Heavy Metals in Fish (Barbodes sp.) Tissues in the Brantas River, Indonesia, Journal of Applied Environmental and Biological Sciences 7(3): 139-143.

Khan H., Ullah H., and Nabavi S.M., (2019). Mechanistic Insights of Hepatoprotective Effects of Curcumin: Therapeutic Updates and Future Prospects, Food and Chemical Toxicology 124: 182–191.

Lee K., Aziz F.H., Syahida A., Abas F., Shaari K., Israf D.A., and Lajis N.H., (2009). Synthesis and Biological Evaluation of Curcumin-Like Diarylpentanoid Analogues for Anti-Inflammatory, Antioxidant and Anti-Tyrosinase Activities, European Journal of Medicinal Chemistry 44(8): 3195-3200.

Liu Z., He C., Chen M., Yang S., Li J., Lin Y., Deng Y., Li N., Guo Y., Yu P., and Li X., (2018). The Effects of Lead and Aluminum Exposure on Congenital Heart Disease and The Mechanism of Oxidative Stress, Reproductive Toxicology 81: 93–98.

Molyneux P., (2004). The Use of The Stable Free Radical Diphenylpicrylhydrazyl (DPPH) for Estimating Antioxidant Activity, Songklanakarin Journal of Sciences and Technology 26(2): 211-219.

Nimse S.B., and Pal D., (2015). Free Radicals, Natural Antioxidants, and Their Reaction Mechanisms, RSC Advances 5: 27986-28006.

Priyadarsini K. I., Maity D. K., Naik G. H., Kumar M. S., Unnikrishnan M. K., Satav J. G., and Mohan H. (2003). Role of Phenolic O-H and Methylene Hydrogen on the Free Radical Reactions and Antioxidant Activity of Curcumin, Free Radical Biology and Medicine, 35(5): 475-484.

Raj S., and Shankaran D.R., (2016). Curcumin Based Biocompatible Nano-fibers For Lead Ion Detection, Sensors and Actuators B 226: 318–325.

Shah F.C., and Jain N.K., (2016). Ameliorative Action of Synthetic and Herbal Antioxidants on Lead Induced Hepatotoxicity: An In Vitro Study, Asian Journal of

Pharmaceutical and Clinical Research 9(2) : 364–370.

Sharma S., and Singh B., (2014). Effects of Acute and Chronic Lead Exposure on Kidney Lipid Peroxidation and Antioxidant Enzyme Activities in BALB-C Mice (Mus musculus), International Journal of Science and Research 3(9): 1564-1566.

Sugiharto, Arbakariya A., Syahida A., and Muhajir H., (2013). Properties of Curcumin: Assay of Tyrosinase Activities, Proceeding of 4th ICOWOBAS–RAFSS, UTM–Malaysia, 80–82.

Sugiharto, Arbakariya A., Syahida A., and Muhajir H., (2016). Properties of Kojic Acid and Curcumin: Assay on Cell B16-F1, 5th ICOWOBAS 2015, AIP Conference Proceedings 1718, 060006; https://doi.org/10.1063/1.4943328

Sugiharto, Win Darmanto, and Sri Puji A.W., (2018). Antioxidant Activity of Curcumin on Blood Serum Assay and Liver Cells of Mice, Research Report, Faculty of Sciences and Technology, Airlangga University.

Ugya A.Y., and Imam T.S., (2017). Temporal Heavy Metal Variation in Vegetables Sampled at Kasuwan Mata, Kaduna Metropolis, Nigeria, Malaysian Journal of Science 36(2): 63-74.

Xu J., Lian L.J., Wu C., Wang X.F., Fu W.Y., and Xu L. H., (2008). Lead Induces Oxidative Stress, DNA Damage and Alteration of p53, Bax and Bcl-2 Expressions in Mice, Food and Chemical Toxicology 46(5): 1488-1494.

CRUDE POLYSACCHARIDES EFFECT OF *Coriolus versicolor* ON *Mycobacterium fortuitum*-INDUCED IMMUNE DYSFUNTION IN MICE

Sri Puji Astuti Wahyuningsih[1a*], Dwi Winarni[1b], Win Darmanto[1c], Sugiharto[1d], Elma Sakinatus Sajidah[1e], and Baiq Naili Dewi Atika[1f]

1Department of Biology, Faculty of Science and Technology, Airlangga University, Surabaya 60115, INDONESIA.
Email: sri-p-a-w@fst.unair.ac.id[a]; dwi-w@fst.unair.ac.id[b]; windarmanto@fst.unair.ac.id[c]; sugiharto@fst.unair.ac.id[d]; elmasakinatus@gmail.com[f]; baiq.naili.dewi-2017@fst.unair.ac.id[g]
*Corresponding Author: sri-p-a-w@fst.unair.ac.id
Submitted: 27th December 2018 Accepted: 9th July 2019 Published: 30th November 2019
DOI: https://doi.org/10.22452/mjs.sp2019no3.4

ABSTRACT *Coriolus versicolor* contains crude polysaccharides which have β-glucan active ingredients. It can activate granulocyte, monocyte, and macrophage. Administration of crude polysaccharide of *C. versicolor* against bacterial infection is hypothesized to increase immune response. This study assessed the crude polysaccharides activity of *C. versicolor* in improving immune response after induction of non-tuberculosis mycobacteria, *Mycobacterium fortuitum*. Animal model was female mice strain BALB/c aged 8-10 weeks. A crude polysaccharide of *C. versicolor* was administered before and/or after the bacteria infection for 10 days at a dose of 50 mg/kg body weight. Mice exposure to *M. fortuitum* was performed twice at a dose of 0.5 Mc. Farland. After crude polysaccharides treatment, both serum and peritoneal fluid were isolated. All data collected were analyzed statistically using ANOVA and Duncan test. Oral administration of crude polysaccharide was found to increase phagocyte number ($P<0.05$, from crude polysaccharides administration before-after infection), improve phagocytic activity ($P<0.05$, from crude polysaccharides administration before infection), raise both IFN-γ and antibody level ($P<0.05$, from crude polysaccharides administration after and before-after infection), and it caused TNF-α levels to tend to a normal concentration ($P>0.05$, TNF-α levels after crude polysaccharides administration were relatively the same as controls). Administration of crude polysaccharides of *C. versicolor* could enhance non-specific immune response, specific immune response, and pro-inflammatory cytokine in mice infected by *M. fortuitum.* These results suggested that crude polysaccharides of *C. versicolor* may be applied as an effective immunostimulatory agent.

Keywords: *Coriolus versicolor*, crude polysaccharide, *Mycobacterium fortuitum*, immune function

1. INTRODUCTION

Mycobacterium fortuitum is one of the non-tuberculous mycobacteria that infect the skin, soft tissue, lungs, lymph nodes, and joints in the postoperative section (Atkins and Gottlieb, 2014). The infection is frequently caused by direct or indirect exposure of the wound to contaminated tap water and air (Scheld, 2014). The most frequently reported infections were post-surgical, primary cutaneous, and pulmonary (Lahiri et al., 2009).

The body possesses an immune system against pathogens infecting both cells and tissue. Epithelial cells are the first line of defense as natural immunity. It can produce chemokine and cytokine that activate phagocytic cells to destroy pathogens and infected cells (Paul, 2013). Natural immunity consists of various components, such as a phagocyte, NK cell, mast cell, eosinophil, neutrophil, complementary component, and pro-inflammatory cytokines, for example, interferon (IFN)-γ, interleukin (IL)-1, IL-6, IL-12, IL-18, and tumor necrosis factor (TNF)-α (D'Elios et al., 2011).

In Indonesia, *Coriolus versicolor* mushrooms are abundant and have not been utilized. Some studies state that *C. versicolor* fungus contains polysaccharides, specifically polysaccharide krestin (PSK) that was previously found to possess immunomodulatory activity (Fritz et al, 2015). The carbohydrate compounds consist of mannose, xylose, galactose, in addition to fructose in polysaccharide peptide (PSP) or arabinose and rhamnose in PSK (Ng, 1998). The PSP is typically isolated by boiling COV-1 mycelia or fruiting bodies in water, followed by precipitation in ethanol (Kotsirilos et al., 2011, Saleh et al., 2017). Polysaccharide krestin is composed of β-glucan attached to proteins. Structural analysis revealed that β-glucan from *C. versicolor* has a linear α-glucan chain composed of only (1→ 6)-α-D-Glcp. It has a glucose homopolymer associated with glycoside bond (Awadasseid et al., 2017). It can interact with immune cells to produce both cytokines and endogenous antioxidant (Chen and Seviour, 2007) so to improve immune response (Meena et al., 2013). Macrophage as the non-specific immune cell can degrade β-glucan into smaller fragments and then released into lymphoid tissue, such as bone marrow, lymph, and lymph nodes (Goodridge et al., 2009).

Beta-glucan fragment activated granulocyte, monocyte, macrophage, natural killer (NK) cell, and dendritic cell passing through lymphoid tissue by binding to dectin-1, Toll-like receptor (TLR)-2/6, and complement receptor (CR)-3 (Chan et al., 2009). The interaction of immune cells and β-glucan triggered macrophage and monocyte to produce various cytokines (TNF α, IL-2, IL-10, and IL-12) (Taylor et al., 2004). These cytokines stimulated granulocyte monocyte colony-stimulating factor (GM-CSF) and monocyte colony-stimulating factor (M-CSF) in the bone marrow to improve the proliferation of granulocyte and monocyte, thus increasing the phagocytosis process. The rise of phagocytosis level would produce more nitric oxide (Ushach and Zlotnik, 2016). Cytokine interacted with CR3 to induce NK cells to lyses pathogen-infected cells, meanwhile dendritic cells produced cytokine and triggered T cell proliferation. Cytokine and T-cell activity, then triggered B-cell to produce antibody. Beta-glucan could also modulate Th1 cells to secrete IFN-γ via MHC II mechanism (Chan et al., 2009).

PSK extracted from *C. versicolor* extract had been studied previously as treatment for cancer due to its presumed immunomodulatory effect (Fritz et al, 2015). However, research on the use of polysaccharides from *C. versicolor* to increase immunity against bacterial infection is still scant. Hence, current research was conducted to evaluate the immunomodulatory activity of *C. versicolor* hot water extract against bacterial infection. The present study explored this effect by evaluating phagocyte numbers, phagocytic activity, cytokine production, and antibody level in mice exposed to *M. fortuitum*.

2. MATERIALS AND METHODS

2.1 Preparation of bacteria

M. fortuitum was obtained from Balai Besar Laboratorium Kesehatan, East Java, Indonesia and grown on solid medium at room temperature. Subsequently, *M. fortuitum* was subcultured into 20 mL liquid medium for 2 days. A liquid medium containing bacteria were centrifuged at 3000 rpm for 10 min. The supernatant was discarded, while the pellet was diluted with saline solution at a concentration of 0.5 Mc. Farland.

2.2 *Preparation of crude polysaccharides from C. versicolor*

C. versicolor were collected in June 2016 from teak forests in the Lamongan region, East Java. It has been identified by the Indonesian Institute of Sciences or Lembaga Ilmu Pengetahuan Indonesia (LIPI) Purwodadi, Indonesia (LIPI-14010). *C. versicolor* (4 kg) was air-dried before cut into small pieces and dried in oven at 40^{o}C for 24 h. Mushroom pieces (1 kg) were then ground into powder (500 g). The mushroom powder (200 g) was macerated twice with 3 L and 1 L of hot water at 80-95^{o}C for 2-3 hours. Furthermore, the mushroom extract was filtered using Whatman paper No. 41, vacuum and Buchner funnel. Then, the supernatant was lyophilized. The lyophilized mushroom (20 g) was precipitated by ammonium sulfate 90% for 24 h at 4^{o}C, followed with centrifuge at 9000 rpm for 20 min at 4^{o}C. The precipitated material was dissolved with 10 mL dH_2O, dialyzed overnight and lyophilized to freeze dry. This process produced a powder containing the crude polysaccharides (Cui and Christi, 2003).

2.3 Measurement of the total polysaccharides

The total polysaccharides contents were determined using the phenol-sulfuric acid. The 1.5 g of the powder containing the crude polysaccharides was added to 50 mL of dH_2O as a stock solution. The stock solution (10 µL) was added to 90 µL dH_2O and 50 µL 5% phenol. The solution was homogenized for 1 min, 2 mL of sulfuric acid was then added to the solution before it was incubated for 10 min at room temperature. The blank solution was made from 50 µL 5% phenol and 100 µL of distilled water. Absorbance or optical density (OD) was measured at 490 nm. The OD value obtained was 1.93. It was calculated based on a standard curve (Y = 0.008X + 0.079, Y was OD value D, X was the polysaccharides contents), which resulted 231.4 mg/mL.

2.4 Animal model and experimental design

All procedures involving animal care were approved by the Animal Care and Use Committee (ACUC) of Veterinary Faculty, Airlangga University, Surabaya, Indonesia, number 654-KE. The mice used as animal model were placed in ventilated cages given condition of 12-h light/12-h dark cycle. Thirty-six female BALB/c mice (8-10 weeks; 30-40 g) were acclimated for a week before divided into 6 groups: normal control, without crude polysaccharide administration and *M. fortuitum* exposure (K), positive control with administration of crude polysaccharide (K+), negative control which exposed to *M. fortuitum* and without polysaccharide administration (K-), and P1, P2, P3 with administration of crude polysaccharide before, after, and both before-after exposure of *M. fortuitum* respectively. Crude polysaccharides were administrated at a dose of 50 mg/kg body weight by peroral gavage for 10 days. Exposure of bacterial infection was

performed 2 times intraperitoneally with 2 weeks interval.

2.5 Collection of serum sample

After one week of crude polysaccharide administration, blood was taken from mice by cardiac puncture. Blood was left to coagulate at room temperature for 2 h before centrifuging at 3000 rpm for 10 min. Serum was isolated and used to measure cytokines (IFN-γ & TNF-α) and antibody level.

2.6 Collection of peritoneal fluid

The intraperitoneal cavity of mice was injected with 0.2 mL of *M. fortuitum* suspension. One hour after the injection, mice were anesthetized using ketamine. Saline solution containing 10% EDTA (2 mL) then injected into the intraperitoneal cavity. Finally, 0.5-1 mL intraperitoneal fluid was taken using a syringe to evaluate the number of phagocytes and phagocytic activity.

2.7 Phagocyte number evaluation and phagocytic activity assay

As much as 20 µL peritoneal liquid was diluted with 100 µL Turk solution and resuspended for 10 times until it was well mixed. The solution was dripped onto the right and left margins of the hemocytometer counting chamber, then phagocyte number was counted. Meanwhile, 70 µL peritoneal fluid was smeared on a slide glass and air-dried. The smear was stained using 0.01% carbol fuchsin dye for 30 min. Slides were passed by fire over a Bunsen burner until it was smoked but not boiled. The smear was then cooled down for about 3-5 min. It was next washed in running water and the remaining color was rinsed with 0.1% HCl until no carbol fuchsin dye found left. The smear was washed again with running tap water before counterstained using methylene blue for 3-5 min. Finally, the smear was rinsed using water and then left to dry. Phagocytic activity was measured from the percentage of phagocytes found ingesting bacteria out of 100 phagocytes count.

2.8 Serum cytokines assay

Cytokines measured in this study were IFN-γ and TNF-α. The level of both cytokines was measured using the Sandwich-ELISA method. Microplate initially was coated with either anti-IFN-γ or anti-TNF-α. As much as 100 µL serum was diluted with assay buffer (1:1) then filled into wells and incubated overnight at 4°C. Microplate was emptied over and washed 3 times with washing buffer. Next, 50 µL biotin-conjugate was added into each well. Microplate was incubated at room temperature (18-25^{o}C) covered with aluminum foil for 2 h while it was shaken at 200 rpm. Microplate was then rinsed 3 times with washing buffer. Streptavidin-HRP solution was added into each well, except for blank well. The plate was incubated again at room temperature, covered with aluminum foil for 1 h. Microplate was rewashed 3 times using washing buffer before 100 µL TMB substrate solution was added into each well. The plate was incubated lastly at room temperature for 10 min until the color was formed. A positive reaction was indicated by a dark blue color. The reaction was discontinued by adding 100 µL stop solution into each well. The value of optical density (OD) was determined using an ELISA reader at 450 nm wavelength. Both IFN-γ and TNF-α levels were converted from OD value using a standardized curve.

2.9 Antibody level assay

The antibody level was measured using indirect ELISA method. Antibody level was determined from OD value. A total of 100 µL bacteria firstly coated onto 96-

well microplate and incubated overnight at 4°C. Blocking was performed by adding 200 µL 10% BSA solution before microplate was incubated for 15 min at room temperature. Each well was then added 100 µL primary antibody and incubated for 1 h at room temperature. The microplate was washed 3 times with washing buffer, then 100 µL of 1 µg/mL conjugate of IgG goat anti-mouse was added into each well. Microplate was incubated again for 1 h at room temperature before it was rinsed 3 times using a washing buffer. Finally, each well was added 100 µL ABTS substrate and left to react. The reaction was stopped by adding 100 µL stopping solution. The OD value of antibody was determined using a microplate reader at 405 nm wavelength.

2.10 Statistical analysis

All values are expressed as mean ± standard error (SE). Statistical analysis was performed using one-way ANOVA followed by Duncan multiple comparison test. All analysis was performed using IBM SPSS Statistics 24 software. P-values less than 0.05 were considered statistically significant.

3. RESULTS AND DISCUSSION

3.1 Effect of crude polysaccharides of C. versicolor on the number of phagocytes

Effect of crude polysaccharides of *C. versicolor* on the number of phagocytes was presented in Fig. 1. The number of phagocytes in K, K+, K-, P1, P2, and P3 groups were 99±25, 90±29, 100±25, 88±44, 86±18, and 180±37 ($x10^5$cell/mm^3), respectively. It was significantly increased in the P3 group compared to other groups ($P<0.05$). Meanwhile, the phagocyte number from P1 and P2 was found to be relatively similar and did not show a significant difference compared to K, K+, and K- ($P>0.05$).

Phagocytes are an important part of the body's defense system and counting the number of phagocytes is a valid method to evaluate immune function (Abbas et al., 2014). Phagocytic cells of the immune system consist predominantly of macrophage and neutrophil. These cells represent major cellular effectors of non-specific host defense and inflammation. Through their ability to phagocytize foreign substances and release cytotoxic and pro-inflammatory mediators, neutrophil and macrophage protect the body from a wide array of pathogens and xenobiotic while also play a central role in the host response towards tissue injury (Laskin et al., 2010). A decrease in the number of phagocytes causes disorders of certain immune factors, leading to a decrease in immune function. The administration of *Schisandra* polysaccharides significantly inhibits the decrease in phagocytes in mice immune compromised with cyclophosphamide (Yu et al, 2018).

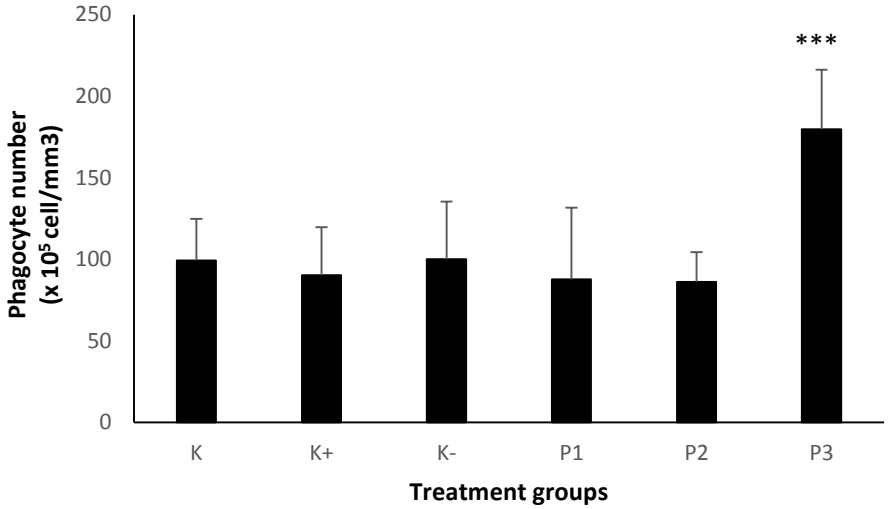

Figure 1. Effect of *crude polysaccharides* of *C. versicolor* on number of phagocyte. K: normal control; K+: positive control; K-: negative control; P1, P2, and P3: treated with *C. versicolor* extract before, after, and before-after exposure of *M. fortuitum.* ***) P<0.05, compared to K, K+, and K-.

The results of the present study indicated that crude polysaccharide of *C. versicolor* significantly inhibits the decrease in the number of phagocytes in mice immune dysfunction induced *M. forfoitum.* The number of phagocytes increased in group-administered *C. versicolor* extract before-after bacterial infection (P3 group). Saleh et al. (2017) have reported that polysaccharide extracted from *C. versicolor* was able to enhance the proliferation of leukocyte. Ng (1998) stated that PSK activity is characterized by their ability to increase white blood cell counts, IL-2 production and delayed-type hypersensitivity reactions. Also, the treatment of healthy nude mice (i.p.) with *C. versicolor* extract for 2 weeks resulted in an increased white blood and neutrophil count (Sze and Chan, 2009).

3.2 Effect of crude polysaccharides of C. versicolor on phagocytic activity

Effect of crude polysaccharides of *C. versicolor* on phagocytic activity was presented in Fig. 2. The phagocytic activity was significantly elevated in both P1 (43.6±15.3%) and P2 (40.0±6.2%), which were given extracts before and after bacterial infection compared to positive (25.4± 8.8%) and negative control (30.6±8.4%) (P<0.05). The highest increase of phagocytic activity was found in the P1 group. Meanwhile, P3 (25.7±6.3%) did not show a significant difference compared to normal (24.6±5.2%), positive, and negative control (P>0.05).

Phagocytes are immunocompetent cells that able to destroy microbes by phagocytosis. When the body is infected by the pathogen, phagocytes will be activated due to lipopolysaccharide (LPS) composing bacterial cell wall. Pathogen entering the body will be bound by surface receptors of the phagocyte. Further, phagocyte membranes will surround the pathogen and form phagosomes. It will fuse with lysosomes to form phagolysosomes in which reactive oxygen species (ROS), nitric oxide (NO) and lysosomal enzyme are secreted to destroy bacterial wall and DNA (Abbas et al., 2014).

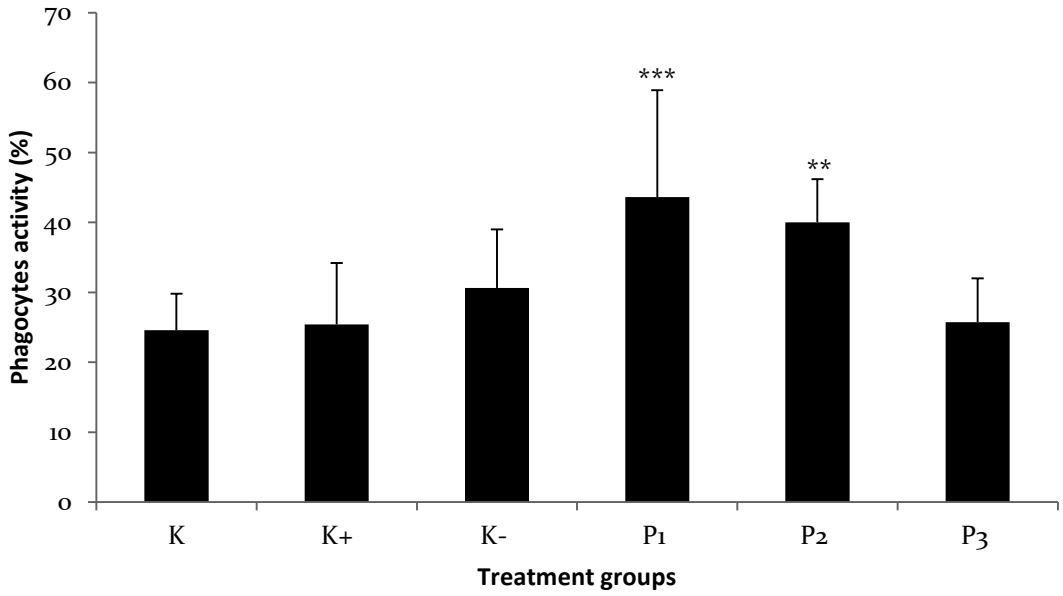

Figure 2. Effect of *crude polysaccharides of C. versicolor* on phagocytic activity. K: normal control; K+: positive control; K-: negative control; P1, P2, and P3: treated with *Coriolus versicolor* hot water extract before, after, and before-after exposed to *M. fortuitum.* **) $P<0.05$ compared to K and K+. ***) $P<0.05$ compared to K, K+, and K-.

Phagocytic activity was found to increase in groups infected by *M. fortuitum* (K-, P1, P2, and P3). This infection would induce proliferation of phagocytic cells, then induction occurred again when *C. versicolor* extract was administrated before and/or after bacterial infection. Saleh et al. (2017) stated that binding of PSK to any/all of Dectin-1, CR3, or TLRs on macrophages leads to the activation of genetic events that increase phagocytic activity and induces the production of oxidative radicals. Then, the phagocytosis process will occur against the antigen from the outside. Vetvicka and Oliveira (2014) reviewed that β-glucan content in carbohydrate was considered a non-specific stimulator of cellular immunity, particularly macrophage. Chen et al. (2008) reported that β-glucan was also found to upregulate phagocytosis of macrophage after bacterial infection in chicken. Novak and Vetvicka (2008) research showed that β-glucan increased both proliferation of macrophage and cytokine in bone marrow, thus more phagocytes were recruited to the infected organs. Wahyuningsih et al. (2016) stated that polysaccharide krestin from *C. versicolor* increased both phagocytic activity and capacity on *Mus musculus* exposed to *Pseudomonas aeruginosa.* A crude polysaccharide from okra pods could also enhance phagocytic activity (Wahyuningsih et al., 2018).

3.3 Effect of crude polysaccharides of C. versicolor on cytokines production

Serum IFN-γ level was found to increase significantly both in P2 and P3, in which *C. versicolor* hot water extract was administrated with extract after (377.8±68.0 pg/ml) and before-after *M. fortuitum* infection (264.9±122.6 pg/ml) compared to K and K+, but did not significantly differ compared to the negative control (K-) ($p>0.05$). TNF-α level from P1, P2, and P3 did not indicate a significant difference compared to either normal, positive, or negative control

($p>0.05$). A slight decrease of serum TNF-α level was found in P1, P2, and P3, but did not show significant difference statistically. Effect of crude polysaccharides of *C. versicolor* on cytokines production was presented in Table 1.

Nontuberculosis mycobacteria (NTM)-related infection is acquired through environmental exposure. There had been no documented case of human-to-human or animal-to-human transmission. An abnormal immune system, for example, declined $CD^{4+}T$ cell count or macrophage dysfunction, cause susceptibility to NTM infection. Similar to other intracellular pathogens, NTM is phagocytized and destroyed by normal functioning macrophage in response to IFN-γ production, which in turn was upregulated by interleukin-12 (IL-12) (Griffith et al., 2007). In this study, *M. fortuitum* infection also induced IFN-γ release. After the administration of *C. versicolor* extract, the IFN-γ level was increased, especially in P2 and P3.

Tumor necrosis factor (TNF)-α is a mediator of the acute inflammatory response to bacteria. Large amounts of this cytokine may be produced during infections with gram-negative and gram-positive bacteria. The concentration of serum TNF-α may be predictive of the outcome of severe bacterial infections (Abbas et al., 2014). TNF-α critical role in the control of infection by intracellular organisms (Keane, 2004). IFN-γ and IL-12 control mycobacteria through upregulated TNF-α, produced predominantly by monocytes/macrophages. Increased risk of NTM infection presents during TNF inhibitor therapy. In this study, TNF-α level was relatively the same across experimental groups. TNF-α level from the group with bacterial infection alone (K-) was slightly higher compared to groups given polysaccharide from *C. versicolor* extract before, after, and before-after infection (P1, P2, P3). This could cause septic shock. Low levels of TNF-α on P1, P2, and P3 were used for macrophage activation and local inflammation.

Table 1. Effect of crude polysaccharides from *C. versicolor* on cytokines production

Group	IFN-γ level (pg/mL)	TNF-α level (pg/mL)
K	39.5 ± 22.8	842,7 ± 244,97
K+	31.0 ± 9.9	613,7 ± 240,17
K-	269.6 ± 125.6	808,0 ± 277,85
P1	147.9 ± 103.2	543,3 ± 292,04
P2	377.8 ± 68.0**	666,1 ± 141,69
P3	264.9 ± 122.6**	536,1 ± 281,67

K: normal control; K+: positive control; K-: negative control; P1, P2, and P3: treated with *C. versicolor* hot water extract before, after, and before-after exposed to *M. fortuitum.* Values are presented as mean ± SD (n = 6). **) $P<0.05$ compared to K and K

From a previous study, crude polysaccharides extracted from okra pods were able to increase TNF-α level at low doses but inhibited it at a high dose (Wahyuningsih et al., 2018). The supplementation β(1-3)(1-6)-D-glucan significantly lowered the TNF-α levels after lipopolysaccharide (LPS) challenge (Vetvicka and Oliveira, 2014). Detrick et al. (2008) and Abbas et al. (2014) mentioned that TNF-α worked on both leukocyte and endothelial. At a moderate level, it played a role in acute inflammatory response. High TNF-α level could cause pathological abnormality in septic shock, a life-threatening condition caused when bacteria enter the bloodstream, is mediated in large part by this cytokine.

3.4 Effect of crude polysaccharides of C. versicolor on antibody level

Optical Density (OD) value of antibody showed an antibody level indirectly. The higher OD value, the higher antibody level. Antibody level was found to significantly rise in both P2 (0.858±0.180) and P3 (0.856±0.104) compared to normal (0.418±0.051), positive (0.429±0.029), and negative (0.515±0.069) control groups ($P<0.05$). The highest increase of antibody level was shown by P2, which was administered with extract after bacterial infection. Meanwhile, slightly decreased of antibody level was found from P1 (0.448±0.046) which was not different statistically compared to normal, positive, and negative control respectively. Effect of crude polysaccharides of *C. versicolor* on antibody level was presented in Fig. 3.

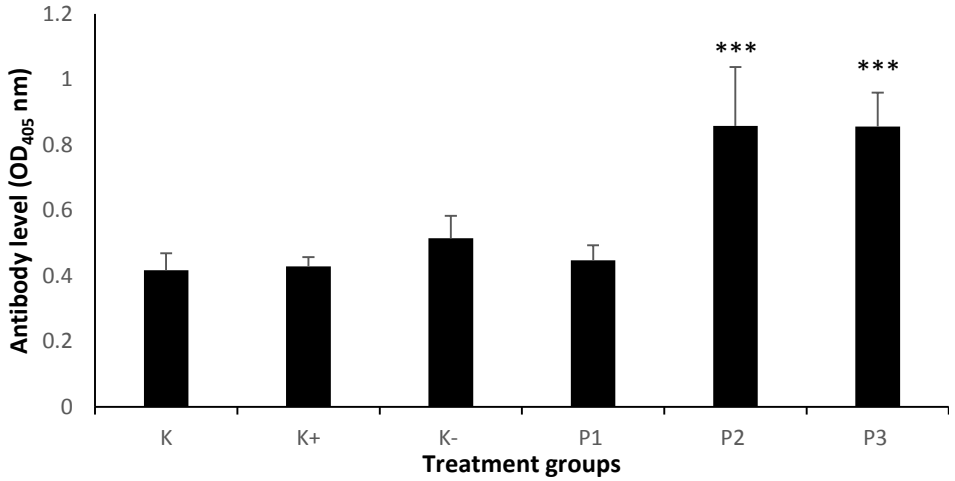

Figure 3. Effect of *crude polysaccharides of C. versicolor* on antibody level. K: normal control; K+: positive control; K-: negative control; P1, P2, and P3: treated with *C. versicolor* hot water extract before, after, and before-after exposed to *M. fortuitum.* ***) $P<0.05$ compared to K, K+, and K-

In this study, the antibody level indicated an increase in P2 and P3, which were given extract after and before-after a bacterial infection, respectively. Saleh et al. (2017) stated that healthy mice treated with polysaccharide peptides from *C. versicolor* for 2 weeks increased B lymphocytes to produce IgG. Recognition of PSK by the B-cell receptor leads to B cell activation, clonal proliferation, and eventual differentiation into IgM or IgG plasma and memory B cells. PSK may similarly act on B cells to T cells,

non-specifically activating them through TLR(s) and leading to a general increase in polyclonal IgM and IgG levels. Yang et al. (2015) showed that compounds of *C. versicolor* have a marked effect on humoral immunity. Murine splenocytes enriched for B lymphocytes and treated with *C. versicolor* extract for 6 days in culture revealed a potent ability to induce IgM production and IgG1 secretion.

Polysaccharide krestin could function as immunomodulatory as it contained 93% β-glucan active compound (Kastin, 2013). This compound was found to be related to main immune system receptors, including TLR-2/6, CR3, and dectin-1. Immune cells targeted by β-glucan are macrophages, NK cells, dendritic cells, neutrophils, and monocytes. Beta-glucan can promote the production of IL-2, IL-6, interferon, immunoglobulin (Ig)-G, also induce T-cell macrophages and lymphocytes (Ley, 2001). In the current study, the administration of polysaccharides from *C. versicolor* hot water extract caused the rise of phagocyte number and activity, IFN-γ and antibody levels in concerning exposure of *M. fortuitum.*

4. CONCLUSION

We concluded that crude polysaccharides of *C. versicolor* are effective in enhancing immune responses through increased phagocytes, phagocytic activity, IFN-γ levels, and antibody levels. The crude polysaccharides also caused TNF-α levels to be normal. The use of established techniques for isolating pure polysaccharides has the potential to produce drugs that are more effective and reduce side effects beyond the target.

5. ACKNOWLEDGEMENT

This study was financially supported by applied research of pre-eminent college or Penelitian Unggulan Perguruan Tinggi (PUPT), No. 951/ UN3.14/LT/2016, April 4th, 2016.

6. REFERENCES

Abbas A K., Litchmann A H., Pober J S. (2014) *Cellular and Molecular Immunology* - 8th edition, Philadelphia: W B. Saunders Company USA.

Atkins B L., Gottlieb T. (2014) Skin and soft tissue infections caused by nontuberculous mycobacteria, *Curr. Opin. Infect. Dis*. 27(2): 137–145.

Awadasseid A., Hou J., Gamallat Y., Xueqi S., Eugene K D., Hago A M., Bamba D., Meyiah A., Gift C., Xin Y. (2017) Purification, characterization, and antitumor activity of a novel glucan from the fruiting bodies of *Coriolus versicolor*, *Plos One*. 12(2): e0171270.

Chan G C., Chan W K., Sze D M. (2009) The effect of β-glucan on human immune and cancer cells, *J. Hematol. Oncol.* 2(25): 1-11.

Chen J., Seviour R. (2007) Medicinal importance of fungal β-(1→3), (1→6)-glucans, *Mycol. Res.* 111(6): 635-652.

Chen K L, Weng B C, Chang M T. (2008) Direct enhancement of the phagocytic and bactericidal capability of abdominal macrophage of chicks by beta-1,3–1,6-glucan,

Poult. Sci. 87(11): 2242-2249.

D'Elios M., Benagiano M., Bella C., Amedei A. (2011) T-cell response to bacterial agents, *J. Infect. Dev. Ctries.* 5(9): 640-645

Detrick B., Nagineni C N., Hooks J. (2008) Cytokines: regulators of immune responses and key therapeutic targets. Gorman MRG, Donnenberg AD. (eds). *Handbook of Human Immunology*, 2nd ed. CRC Press.

Fritz H., Kennedy D A., Ishii M., Fergusson D., Fernandes R., Cooley K., Seely D. (2015) Polysaccharide K and *Coriolus versicolor* Extracts for Lung Cancer: A Systematic Review, *Integr. Cancer. Ther*. 14(3): 201-11.

Goodridge H S., Wolf A J., Underhill D M. (2009) Beta-glucan recognition by the innate immune system, *Immunol. Rev.* 6(1): 33-34.

Griffith D E., Aksamit T., Brown-Elliott B A., Catanzaro A., Daley C., Gordin F. (2007) An official ATS/IDSA statement: diagnosis, treatment, and prevention of nontuberculous mycobacterial diseases, *Am. J. Respir. Crit. Care. Med.* 175(4): 367–416.

Kastin A J. (2013) *Handbook of biologically active peptides*, Academic Press, UK.

Keane J. (2004) Tumor necrosis factor blockers and reactivation of latent tuberculosis, *Clin. Infect. Dis*. 39(3):300–302.

Kotsirilos V., Sali A., Vitteta L. (2011) *A guide to evidence-based integrative and complementary medicine*, Elsevier Health Science Sydney.

Lahiri K K., Jena J., Pannicker K K. (2009) *Mycobacterium fortuitum* infections in surgical wounds, *Med. J. Armed. Forces. India.* 65(1): 91–92.

Laskin D L., Gardner C R., Laskin, J D. (2010) Phagocytes. *Comprehensive Toxicol.* 5:133-153.

Ley B M. (2001) *Discovery the beta-glucan secret*, BL Publications USA.

Meena D K., Das P., Kumar S., Mandal S C., Prusty A K., Singh S K. (2013) Beta-glucan: an ideal immunostimulant in aquaculture (a review), *Fish. Physiol. Biochem.* 39: 431–57.

Ng T B. (1998) A review of research on the protein-bound polysaccharide (polysaccharopeptide, PSP) from the mushroom *Coriolus versicolor* (Basidiomycetes: Polyporaceae), *Gen Pharmacol*. 30(1): 1-4.

Novak M., Vetvicka V. (2008) Beta-glucan, history, and the present: immunomodulatory aspect and mechanisms of action. *J. Immunotoxicol.*, 5(1): 47-57.

Paul W E. (2013) *Fundamental Immunology*, 7th Edition**,** Lippincott Williams & Wilkins USA.

Saleh M H., Rashedi I., Keating A. (2017) Immunomodulatory properties of *Coriolus versicolor*: the role of polysaccharopeptide, *Front. Immunol.* 8(1087): 1-12.

Scheld W M., Whitley R J., Marra C M. (2014) *Infections of the central nervous system*, 4th edition, Philadelphia: Wolters Kluwer Health, USA.

Sze D M., Chan G C. (2009) Supplements for immune enhancement in

hematologic malignancies, *Hematology Am. Soc. Hematol. Educ. Program.* 2009:313–319.

Taylor P R., Brown G D., Herre J., Williams D L., Willment J A., Gordon S. (2004) The role of SIGNR1 and the beta-glucan receptor (dectin-1) in the non-opsonic recognition of yeast by specific macrophages, *J. Immunol.* 172(2): 1157-1162.

Ushach I., Albert Zlotnik A. (2016) Biological role of granulocyte-macrophage colony-stimulating factor (GM-CSF) and macrophage colony-stimulating factor (M-CSF) on cells of the myeloid lineage, *Leukoc Biol*. 100(3): 481–489.

Vetvicka V., Oliveira C. (2014) β(1-3)(1-6)-D-glucans modulate immune status in pigs: potential importance for efficiency of commercial farming, *Ann. Transl. Med*. 2(2): 16.

Wahyuningsih S P A., Savira N I I., Darmanto W. (2016) Effect of polysaccharide krestin from *Coriolus versicolor* on phagocytic activity and capacity of *Mus musculus* exposed *Pseudomonas aeruginosa*, *Biosaintifika: Journal of Biology & Biology Education*. 8(3): 308-313.

Wahyuningsih S P A., Pramudya M., Putri I P., Savira N I I., Winarni D., Darmanto W. (2018) Crude polysaccharides from okra pods (*Abelmoschus esculentus*) grown in Indonesia enhance the immune response due to bacterial infection, *Adv. Pharmacol. Sci.*, 2018(4) ID 8505383.

Yang S F., Zhuang T F., Si Y M., Qi K Y., Zhao J. (2015). *Coriolus versicolor* mushroom polysaccharides exert immunoregulatory effects on mouse B cells via mem-brane Ig and TLR-4 to activate the MAPK and NF-kappaB signaling pathways, *Mol. Immunol.* 64(1): 144–51.

Yu J., Cong L., Wang C., Li H., Zhang C., Guan X., Liu P., Xie Y., Chen J., Sun J. (2018). Immunomodulatory effect of *Schisandra* polysaccharides in cyclophosphamide‐induced immune-compromised mice, *Exp. Ther. Med.* 15(6): 4755-4762.

AUTOMATIC IDENTIFICATION OF RING ENHANCING LESION PATTERN IN CASES OF BRAIN INFECTION AND METASTASIS BRAIN TUMOR BASED ON INVARIANT MOMENT FEATURES CLASSIFICATION

Riries Rulaningtyas[1a*], Lailatul Muqmiroh[2b], Leonard Ferdian[1c], Abidah Alfi[1d], Isma Iba[1e]

[1]Biomedical Engineering Study Program, Department of Physics, Faculty of Science and Technology, Universitas Airlangga, Jalan Mulyorejo, Surabaya, 60115, INDONESIA. E-mail: riries-r@fst.unair.ac.id[a]; lailatul.muqmiroh@vokasi.unair.ac.id[b]; leo@dataku.web.id[c]; rigeliastar@gmail.com[d]; ismaiba97@gmail.com[e]
[2]Radiologic Technology Program, Faculty of Vocational Studies, Airlangga University, Jalan Dharmawangsa Dalam 25-30, Surabaya, 60286, INDONESIA, E-mail: liling.sahadi@gmail.com[b]
*Corresponding Author: riries-r@fst.unair.ac.id
Submitted: 31st December 2018 Accepted: 15th October 2019 Published: 30th November 2019
DOI: https://doi.org/10.22452/mjs.sp2019no3.5

ABSTRACT Brain infection and metastasis brain tumor in CT Scan examination have similar ring-enhancing lesion patterns. This research aims to develop a program that aids the radiologists to identify these brain disorders. The radiologists often have difficulties and mostly subjective when distinguishing the ring-enhancing lesion whether brain infection or metastatic brain tumor, especially in patients with no previous history of the disease. With these limitations, this research produces a Computer Aided Diagnose (CAD) system in order to assist the radiologists in brain disorders observing from the images of CT scan brain scanning. The CAD system is supported by features extraction method which is generated using the combinations of Hu's invariant moment features. The decision maker uses the backpropagation neural network method to classify the brain disorders based on their invariant moment features that could help the radiologists when identifying the brain abnormalities. The results of brain abnormalities identification including normal, brain infection, and metastasis brain tumor yielded performance with 88.9% accuracy, 86% sensitivity, and 100% specificity.

Keywords: CT scan, identification, invariant moment features, backpropagation, neural network.

1. INTRODUCTION

Brain infection and metastasis brain tumor are serious diseases with high number of cases. Radiology imaging is an important part for brain abnormalities diagnosis. The most frequently used radiology instruments for the diagnosis of brain tumor and metastasis brain tumor are CT Scan and Magnetic Resonance Imaging (MRI). MRI has an ability to distinguish brain infection and metastasis brain tumor more accurately and appears to be clearer shape than CT Scan in those two brain abnormalities with similar shapes with multiple ring enhancing. The most imaging modality that used in the hospital is CT Scan because the CT Scan has lower cost than MRI. Lesions that describes the infection process or metastases in the brain on CT scan seen as a ring enhancing lesion after given contrast. The radiologists often have difficulty to distinguish ring enhancing lesion from CT Scan images, an infection process, or metastases especially

on patients with unknown illness history before. With those limitations, a type of research is needed to diagnose CT scan image with image processing method so that the radiologist can distinguish various kind of brain abnormalities such as infection and metastatic tumors in brain.

In this research, we use appropriate pattern recognition methods to distinguish the object of ring lesions in brain resulted from CT Scan scanning with two kinds of classification whether brain infection or metastasis brain tumor. In this study, we use Hu's moment invariant that can measure the quantities of the particular differential pattern which has the discriminant power to differentiate the pattern between these two abnormalities brain diseases.

Zhang et al (2015) used Hu's moment invariant as feature extraction with classification accuracies of 100% over Dataset-66, 100% over Dataset-160, and 99.45% over Dataset-255. Zunic, et al (2010) used Hu moment invariants that could detect small irregularities in nearly circular shapes broken by noise. Moment invariant is proven to have high ability to trace the pattern of images with images translation, scaling, rotation, and free from noise (Huang & Leng, 2010), hence this research uses the Hu's moment invariant as feature extraction and backpropagation neural network as the classification method. But before that, an image processing method is conducted which consists of preprocessing and segmentation. Feature extraction for this research used 7 combination of Hu's moment invariant method and the backpropagation neural network method classifies the characteristics from a unique object to represent the shape to distinguish the two of brain abnormalities cases with feature extraction of a ring enhancing shape on infection and metastatic. All data that will be processed in this research is a data result of CT Scan modality test. Generated data will be in the form of images with various kind of gray intensity that describes brain structure along with abnormalities (lesions) for brain infection and metastatic cases.

2. THE RING ENHANCEMENT LESION PATTERN

The ring enhancing pattern is a difficult pattern to be analyzed in neuroimaging, especially in the metastasis brain tumor and brain infection images that resulted from CT Scan. The lesion pattern of both brain abnormalities are similar each other that form the ring enhancement pattern. This ambiguity pattern can cause the decreasing accuracy of the radiologist diagnosis, even less the patients do not have the exact previous symptoms.

The pattern of ring lesion in the brain infection has the ring with smooth line, but in the metastasis brain tumor has rough and irregular line shapes. The Figure 1(a) represents the ring lesion pattern of brain infection and (b) malignant brain tumor. The radiologists have difficulties to distinguish both these patterns visually from CT Scan images. In some cases, these brain abnormalities show the multiple ring enhancing lesions as shown in Figure 2.

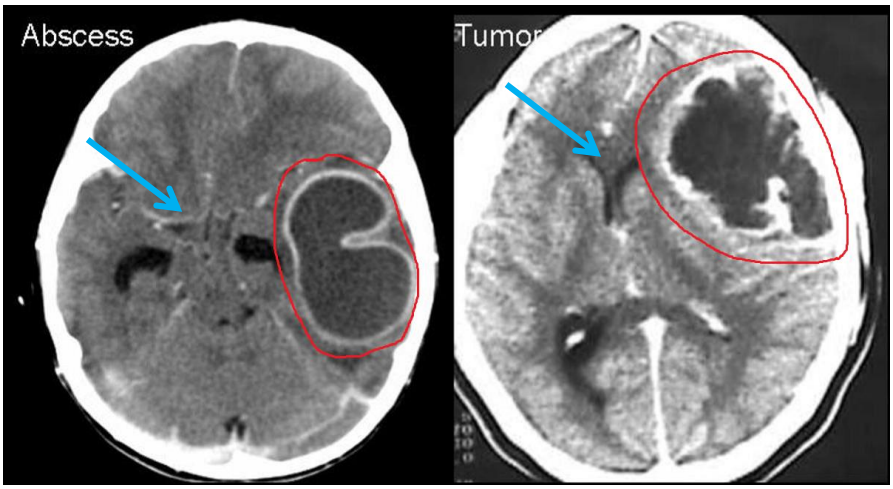

(a) (b)

Figure 1. The Ring Enhancing Lesion Pattern
(a) In The Brain Infection (b) In The Brain Tumor (Claussen *et al*, 1982)

The ring pattern in Figure 3 sometimes is similar with the pattern of Glioblastoma and metastasis.

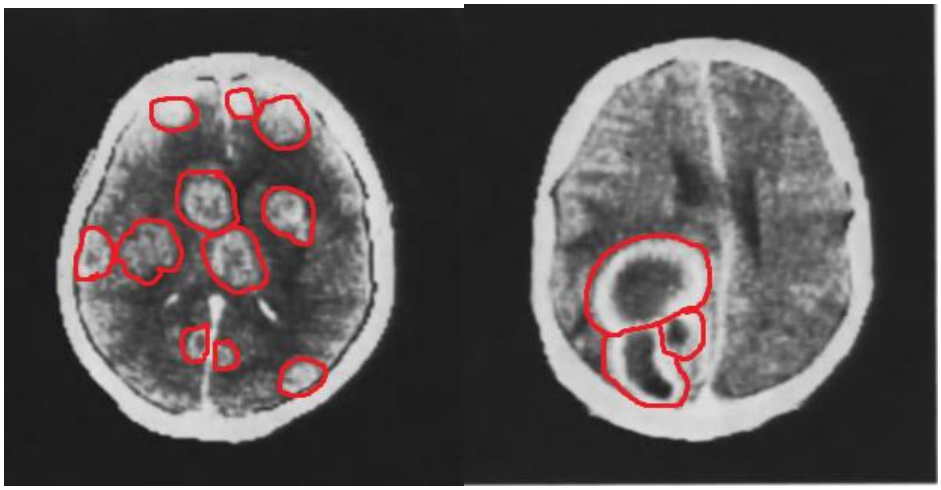

(a) (b)

Figure 2. The Multiple Ring Enhancing Lesions in (a) The Metastasis Brain Tumor (b) The Brain Infection (Claussen *et al*, 1982)

3. THE HU MOMENT INVARIANTS

Moment Invariant is introduced by Hu that formulate the six absolute orthogonal invariants and an orthogonal invariant based on algebraic invariants. The 2-D moment with order $(a+b)$ in the digital image $g(m,n)$ is defined as (Zhang, 2016) :

$$moment_{ab} = \sum_m \sum_n m^a n^b g(m,n) \quad (1)$$

Where :

$moment_{ab} = the$ moment of digital images

a,b = the moment order

g = the value of image intensity

m,n = the pixel coordinate

For *a,b* = 0, 1, 2, ..., where the sum of (*a*+*b*) order is above the value of *m* and *n* image's spatial coordinate. The *central moment* is defined as (Zhang, 2016)

$$\varphi_{ab} = \sum_m \sum_n (m - \bar{m})^a (n - \bar{n})^b \, g(m,n) \quad (2)$$

Where $\bar{m} = \frac{A_{10}}{A_{00}} \; dan \; \bar{n} = \frac{A_{01}}{A_{00}}$ (3)

A_{00} = area of whole images

A_{10} = area of the object in the horizontal direction

A_{01} = area of the object in the vertical direction

φ = center moment

$\bar{m}, \bar{n}$ = center image

The Normalized central moment from the order (*a*+*b*) is defined as :

$\psi_{ab} = \frac{\varphi_{ab}}{\varphi_{00}^{\beta}}$, for *a, b* = 0, 1, 2, …

where :

$\beta = \frac{a+b}{2} + 1$, for *a*+*b* = 2, 3, ...

The 7 *moment invariants* which are not sensitive to the translation, scale change, and rotation are derived as (Zhang, 2016) :

$$\Theta_1 = \psi_{20} + \psi_{02} \quad (4)$$

$$\Theta_2 = (\psi_{20} - \psi_{02})^2 + 4\psi_{11}^2 \quad (5)$$

$$\Theta_3 = (\psi_{30} - 3\psi_{12})^2 + (3\psi_{21} - \psi_{03})^2 \quad (6)$$

$$\Theta_4 = (\psi_{30} + \psi_{12})^2 + (\psi_{21} - \psi_{03})^2 \quad (7)$$

$$\Theta_5 = (\psi_{30} - \psi_{12})(\psi_{30} + \psi_{12})[(\psi_{30} + \psi_{12})^2 - 3(\psi_{21} + \psi_{03})^2] + (3\psi_{21} + \psi_{03})(\psi_{21} + \psi_{03})[3(\psi_{30} + \psi_{12})^2 - (\psi_{21} + \psi_{03})^2] \quad (8)$$

$$\Theta_6 = (\psi_{20} - \psi_{02})[(\psi_{30} + \psi_{12})^2 - (\psi_{21} + \psi_{03})^2] + 4\psi_{11}(\psi_{30} + \psi_{12})(\psi_{21} + \psi_{03}) \quad (9)$$

$$\Theta_7 = (3\psi_{21} - \psi_{03})(\psi_{30} + \psi_{12})[(\psi_{30} + \psi_{12})^2 - 3(\psi_{21} + \psi_{03})^2] + (3\psi_{21} + \psi_{03})(\psi_{21} + \psi_{03})[3(\psi_{30} + \psi_{12})^2 - (\psi_{21} + \psi_{03})^2] \quad (10)$$

4. NEURAL NETWORK

Artificial neural network is an algorithm system that has characteristics similar to human nerve tissue. Backpropagation is a supervised learning algorithm and is used by many layers of perceptrons to change the weights connected to neurons in the hidden layer. Figure 3 shows the Backpropagation network architecture.

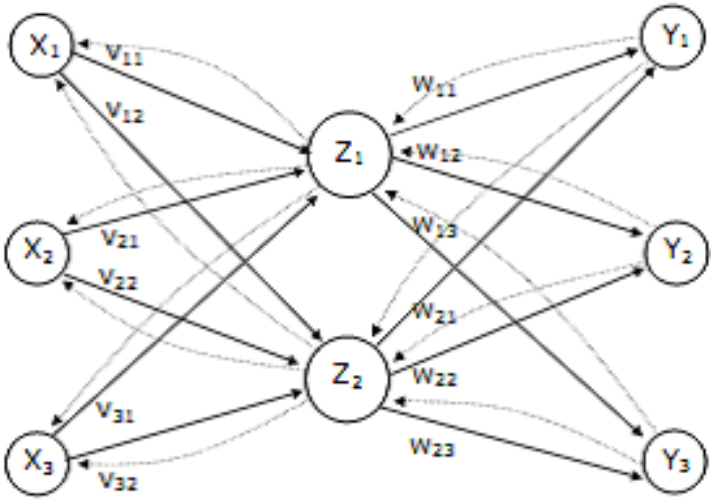

Figure 3. Backpropagation network architecture (Sun, 2016)

5. EXPERIMENTS

5.1 Method

In order to identify ring enhancing lesion in brain metastases and infection, we used images that were acquired from CT scan. Computed Tomography (CT) usually called Computed Axial Tomography (CAT), Computer-assisted Tomography, or (body section rontgenography) uses digital processing to generate an internal three dimensions image of an object from x-rays that will generates two-dimension image. CT scan could give one tumor tissue image with another. CT scan could also give lesions density abnormalities image, and could be clarified by giving contrast (Dewi, Loho, & Tubagus, 2015).

Variety of CT Scan data used in this research are images of brain infection, metastases, and normal condition which have been examined by radiologists. The image data used in this research is DICOM (.dcm) which was the original image acquired from CT Scan instrument. Image obtained has size of 512x512 pixels, and was taken from CT-Scan multislice instrument with maximum X-ray generator of 120 kV.

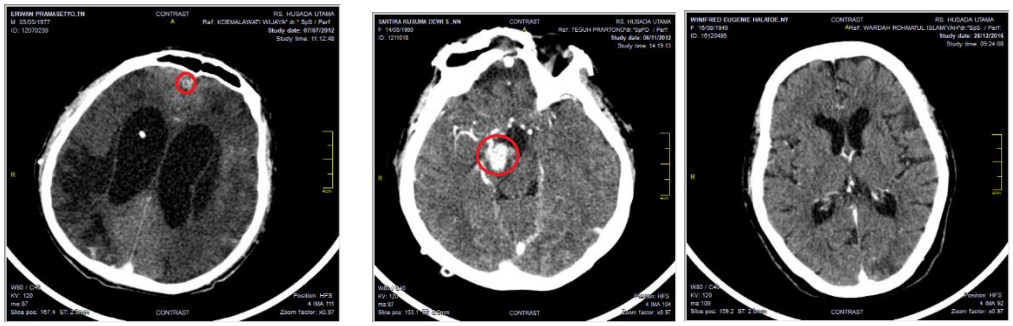

(a) (b) (c)

Figure 4. The Sample Data CT Scan, (a) Brain Infection (b) Metastasis Brain Tumor (c) Normal Brain

All of the data are categorized into training data and test data. 70% of the data are clustered into training data, which includes 25 infection cases, 30 metastases cases, and 50 normal cases. While the rest are testing data which includes 25 infection cases, 25 metastases cases, and 25 normal cases. The Hu moment invariants (ϕ_1 until ϕ_7) of each data images are calculated to become the input of neural network. The backpropagation neural network algorithm that used in this research are (Rulaningtyas, et al, 2011) :

1. Step 0: Initialize weight and bias (random)
2. Step 1: If stopping condition is still not met, run step 2-9
3. Step 2: For each training data, do steps 3-8
4. Step 3: Each input unit (xi, i = 1, ..., n) receives the input signal xi and spreads the signal to all units in the hidden layer
5. Step 4: Each hidden unit (zi, j = 1, ..., p) will add the input signals that have weighted, including the bias.

   $$z\_in_j = v0_j + \sum_{i=1}^{n} x_i v_{ij} \quad (11)$$

   and use the activation function of the hidden unit,

   $$z\_in_j = v0_j + \sum_{i=1}^{n} x_i v_{ij} \quad (12)$$

   then send this output signal to all units
6. Step 5: Each unit of output (yk, k = 1, ..., m) will add the input signals that have weighted, including the bias,

   $$y\_in_k = w0_k + \sum_{j=1}^{p} z_j w_j k \quad (13)$$

   and use the activation function of the output unit concerned,

   $$y_k = f(y_{in_k}) \quad (14)$$
7. Step 6: Each output unit (yk, k = 1, ..., m) accepts a target (expected output) that will be compared to the output produced.

   $$\delta_k = (t_k - y_k) f'(y_{in_k}) \quad (15)$$

   This δk factor is used to calculate error correction (Δw_{jk}) which will later be used to update time, where

   $$\Delta w_{jk} = a\delta_k z_j \quad (16)$$

In addition, the bias correction Δw_{0k} is calculated which will be used to update Δw_{0k}, where

$$\Delta w_{jk} = a\delta_k \quad (17)$$

This δk factor is sending to the layer in front of it.

8. Step 7: Each hidden unit (zj, j = 1, ..., p) sums up the delta input (which is sent from the layer in step 6) which is already weighted.

$$\delta\_in_k = \sum_{k=1}^{m} \delta_k w_{jk} \quad (18)$$

Then the results are multiplied by the derivative of the activation function used by the network to generate an error correction factor δj, where:

$$\delta_j = \delta\_in_k f'\left(z_{in_j}\right) \quad (19)$$

This factor δ_j is used to calculate error correction (Δv_{ij}) that will be used to update the v_{ij}, where:

$$\Delta v_{ij} = a\delta_j x_i \quad (20)$$

Δv0j bias correction is also calculated which will be used to update v0j, where:

$$\Delta v_{0j} = a\delta_j \quad (21)$$

9. Step 8: Each unit of output (yk, k = 1, ..., m) will update the bias and weight in each hidden unit

$$w_{jk}(baru) = w_{jk}(lama) + \Delta w_{jk} \quad (22)$$

Likewise for each hidden unit will update the bias and their weight on each input unit.

$$v_{ij}(baru) = v_{ij}(lama) + \Delta v_{ij} \quad (23)$$

10. Step 9: Check the stopping condition

5.2 Result and Discussion

The identification software for brain infection and metastasis brain tumor developed in this research is shown in the Figure 5.

Figure 5. The Visualization of the Resulted Software

The result of feature extraction using Hu moment invariants method is shown in Figure 6. From Figure 6, the values of the Hu moment invariants could be separated into three threshold values, they are 1, 0, and 0.5. It showed that all The Hu moment invariant features have significant and meaningful values to distinguish the brain disease. From the BPNN training process gives the threshold values 1 for brain infection, 0.5 for metastasis brain tumor, and 0 for normal brain. The Hu moment invariants features will be classified using backpropagation neural network with sigmoid activated function that the target value is determined by range number 0 until 1.

The initial weight values of BPNN is random between -1 until 1. The parameters that are chosen to be optimized in BPNN architecture are the number of hidden nodes, the value of learning rate, and the number of maximum epochs. From the experiment shows that the BPNN architecture with 10 nodes hidden, learning rate 0.5, and maximum epochs 10000 are giving the best performance with highest accuracy (in Figure 7). From MSE (Mean Square Error) graphic in Figure 8, It shows that the error gives the decrease trend until steady state condition reached in the epoch 1000 with MSE 0.0242. For calculating the MSE values, this research used Eq.24.

$$MSE = \frac{1}{b}\sum_{a=1}^{b}(y_{dNN} - y_{oNN})^2 \tag{24}$$

With b : *the number of data*, $y_{dNN} = the\ desired\ neural\ network\ output$, $y_{oNN} = the\ neural\ network\ output$.

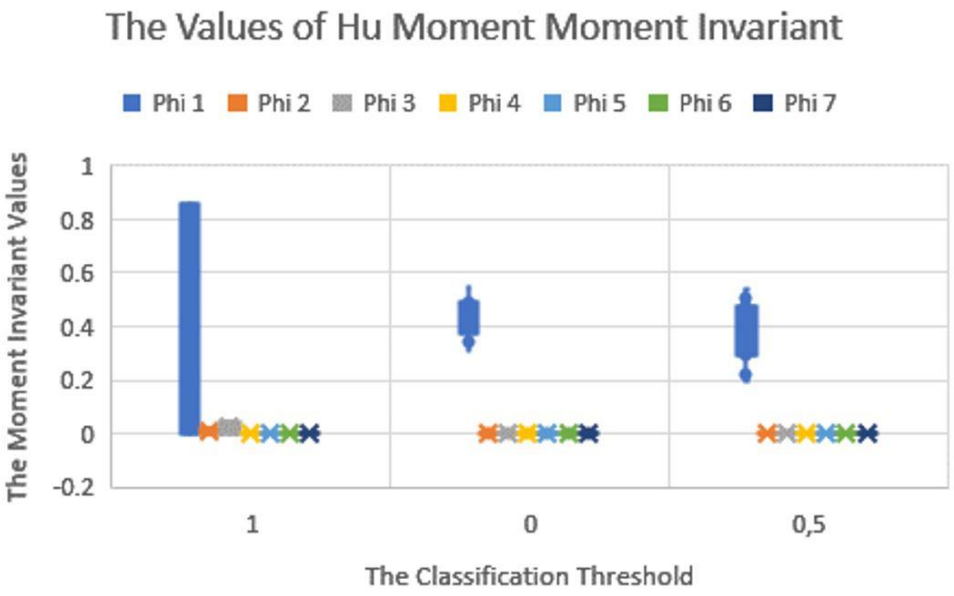

Figure 6. The Hu moment invariants Result

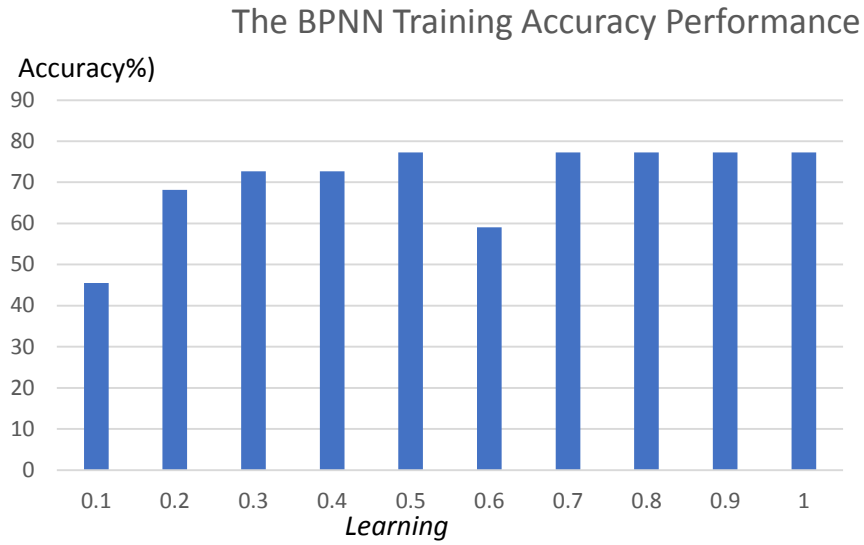

Figure 7. The Comparison of Accuracy Values with the Learning Rate Variation

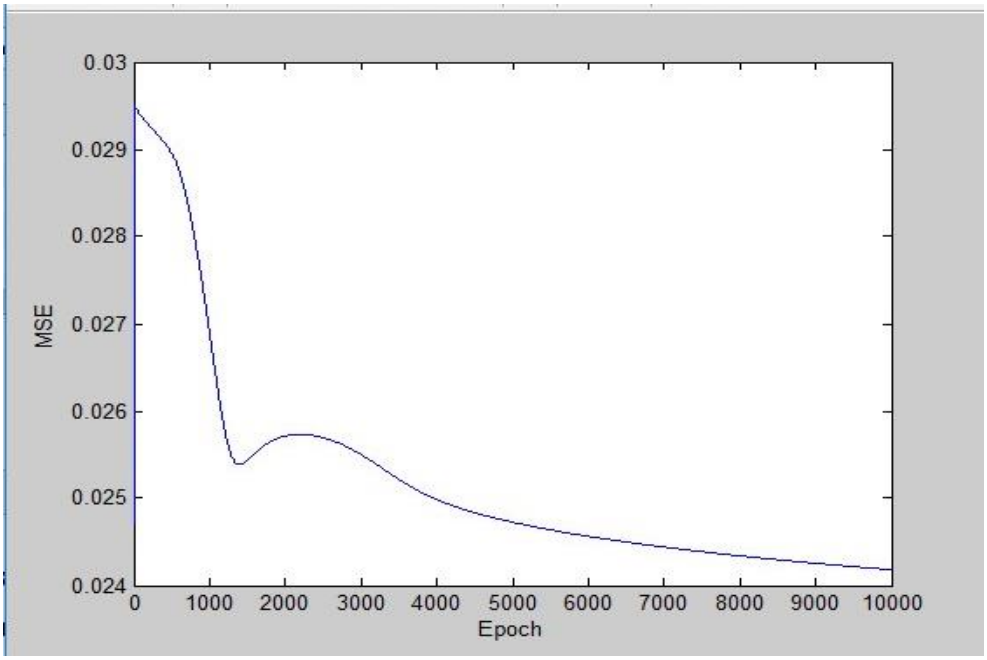

Figure 8. MSE Values from BPNN Training

The measured parameter for succeed classification process is derived by calculation of the accuracy, sensitivity, and specificity values when all the data training and testing compared with the golden standard from the doctors and clinicians. The summary of the research result is represented in Table 1.

$$Accuracy = \frac{T_P + T_N}{P + N} \times 100\% \quad (25)$$

$$P = T_P + F_N \; dan \; N = F_P + T_N \quad (26)$$

$$Sensitivity = \frac{T_P}{T_P + F_N} \times 100\% \quad (27)$$

$$Specificity = \frac{T_N}{F_P + T_N} \times 100\% \quad (28)$$

Where :

T_P = *True positive*

T_N = *True negative*

F_P = *False positive*

F_N = *False negative*

The accuracy represents that the resulted software could classify the all features between normal, brain infection, and metastasis brain tumor cases. The sensitivity represents that the resulted software could classify the features between the normal brain and abnormal brain. The specificity represents that the resulted software could classify the ring features between the brain infection and metastasis brain tumor properly.

Table 1. The Summary of Research Result

The Parameters	The Values
Mean Square Error BPNN	0.0242
Accuracy	88.9%
Sensitivity	86%
Specificity	100%

6. CONCLUSION

Hu moment invariants can identify the pattern of ring enhancing lesion in brain infection and metastasis brain tumor with good accuracy. Hu moment invariants could not be influenced by the position, scale, and rotation position of the brain images in CT Scan. It extracts suitable features for classification as seen in this research the BPNN could distinguish the brain abnormalities, brain infection and metastasis brain tumor with good result in accuracy, sensitivity, and specificity.

To improve the performance of identifying the ring enhancing lesion, this research still needs more development in pattern recognition method to measure the irregularities in the ring boundary shapes. We can try to use unsupervised machine learning method to overcome this problem. The machine learning will adjust their self adaptively to suit the shape of boundary objects that will be identified.

7. ACKNOWLEDGMENT

We would like to thank to Hajj Hospital Surabaya for providing the CT Scan data and to all the doctors and clinicians who cooperated and supported this research.

8. REFERENCES

Claussen C, R. Fahlbusch, R. Felix, T, Grumme . 1. Heinzerling 1.R. Iglesias. (1982) Computed and Tomography. Springer-Verlag Berlin Heidelberg.Dewi, M., Loho, E., & Tubagus, V. N. (2015). Gambaran CT-scan neoplasma intrakranial di Bagian / SMF Radiologi FK Unsrat RSUP Prof . Dr . R . D . Kandou Manado, *4*(September 2015).

Huang, Z., & Leng, J. (2010). Analysis of Hu's Moment Invariants on Image Scaling and Rotation. *2nd International Conference on Computer Engineering and Technology (ICCET), Volume 7*, 476–480. https://doi.org/10.1109/ICCET.2010.5485542

Rulaningtyas, R, Suksmono, B, Mengko, T, L, R, Putri, S. (2011). Automatic Classification of Tuberculosis Bacteria Using Neural Network. IEEE Xplore, page 1-4.

Sun, W., Xu, Y. (2016). Using a Back Propagation Neural Network Based On Improved Particle Swarm Optimization to Study the Influential Factors of Carbon Dioxide Emissions in Hebei Province, China. Journal of Cleaner Production 112(2016), 1282-1291. Elsevier. Zhang, Y., Yang, J., Wang, S., Dong, Z., & Phillips, P. (2016). Pathological Brain Detection in MRI Scanning via Hu Moment Invariants and Machine Learning. Journal of Experimental & Theoritical Artificial Intelligence, 29(2), 299-312. doi:10.1080/0952813x.2015.1132274.

Zhang, Y., Wang, S., Sun, P., Phillips, P. (2015). Pathological Brain Detection Based on Wavelet Entropy and Hu moment invariants. Bio-Medical Materials and Engineering. Vol.26, Page S1283-S1290. IOP Press.

Zunic, J., Hirota, K., Rosin, P.L. (2010). A Hu moment invariants as A Shape Circularity Measure. Pattern Recognition. Volume 43, Issue 1, Pages 47-57. Elsevier.

UNIVERSITY OF MALAYA-INDONESIAN UNIVERSITIES SYMPOSIUM
2018 UMIND2018 [8-9 NOVEMBER 2018]

FABRICATION AND CHARACTERIZATION OF BREAST PHANTOM BASED ON GELATIN-GLYCERIN-TIO_2 FOR A CONTINUOUS-WAVE DIFFUSE OPTICAL TOMOGRAPHY

N. Ukhrowiyah[1a*], D. Hikmawat[1b], M. Yasin[1c], and R. Yuni[1d]

[1]Department of Physics, Faculty of Science and Technology, Universitas Airlangga, Surabaya 60115, Indonesia. Email: nurilukhrowiyah@fst.unair.ac.id[a]; dyah-hikmawati@fst.unair.ac.id[b]; yasin@fst.unair.ac.id[c]; risayuniastuti@gmail.com[d]
*Corresponding Author's Email: nurilukhrowiyah@fst.unair.ac.id
Submitted: 27th December 2018 Accepted: 9th July 2019 Published: 30th November 2019
DOI: https://doi.org/10.22452/mjs.sp2019no3.6

ABSTRACT In this paper, the fabrication and characterization of breast phantom based on gelatin-glycerin-TiO_2 as breast simulation tissue is proposed and investigated. A sample preparation was done by mixing 3 grams of gelatin per 10 ml of saline. The sample was added with glycerin with four different concentrations of 85%, 90%, 95% and 100% as sample A, B, C and D respectively. The sample D is optimum as it was able to survive at room temperature for 126 hours. Subsequently, sample D was added by TiO_2 given variations of 0.010 grams, 0.015 grams, 0.020 grams and 0.025 grams. All samples were tested for its homogeneity and absorption coefficient using Continuous Wave Diffuse Optical Tomography (CW-DOT) with laser wavelengths of 780, 808 and 830 nm. The results showed that the optimum sample characterization was achieved at wavelength of 830 nm with TiO_2 variation of 0.025 grams. The absorption coefficient breast phantom was obtained at 0.167 mm^{-1}. Phantom based on gelatin-glycerin-TiO_2 can be applied as material replacement of breast for test object in CW-DOT.

Keywords: Breast phantom, gelatin, glycerin, titanium dioxide, and optical tomograph

1. INTRODUCTION

Based on 2013 Basic Health Research data, the prevalence of tumors (benign and malignant) in Indonesia has reached 1.4 per 1.000 population or about 330 people. Breast and cervix are types of cancer that most prevalent with highest mortality. Most cases (50%) and breast cancer deaths (58%) allegedly are due to lack of early detection instrument of breast cancer and health care. Approximately 68.6% of women who are infected by Carcinoma mammae are detected after reaching an advanced stage of local (III A and III B), while at an early stage (I and II) only 22.4% are detected (Azamris, 2006).

One of techniques for early detection of carcinoma mammae that is easily accessible by public is the Near Infrared-

diffuse optical tomography (NIR-DOT). The advantage of NIR-DOT lies on its radiation source used which is in the form of Near Infrared (NIR) that is non-invasive and non-ionizing (Kemsley *et al.*, 2008). Unfortunately, a direct exposure to visible light or NIR on mammae tissue often causes concerns in most women. Therefore, an effort to build early detection equipment with NIR-DOT is needed, such as phantom which is a material replacement to simulate the presence of Carcinoma mammae. Phantom is defined as an object that acts as a simulation to replicate the characteristics of human or animal tissue (Pogue *et al.*, 2006). Phantom can be made of various materials including gelatin, lipid, resins, polyester and polyurethane.

Breast phantom which is based on gelatin has several advantages namely its optical characteristics resemble normal breast tissue (de Grand *et al.*, 2006), it is relatively inexpensive and easy to obtain and non-toxic (Lualdi, 2001). However, gelatin has life cycle that tends to be short and easily damaged, so it is necessary to add glycerin to improve durability. Based on an article written by Firbank and Delphy (1993), phantom materials that can be used to approximate the characteristics of the tissue must have optical characteristics that are scattering and absorbing. These scattering and absorbing characteristics can be determined by adding TiO_2 material. TiO_2 can produce a stable scattering spectrum (Jiang, 2003). Based on the reasons aforementioned, this study is expected to shed light on the breast phantom which is durable, resistant to fungi or microbes while having the characteristics of normal breast tissue that can be evaluated from its physical, mechanical, thermal and optical characteristics.

2. MATERIALS AND METHODS

The materials used in this research include gelatin (cow skin gelatin, Guangdong, China), glycerin (P&G Chemical, Malaysia), TiO_2 powder (Titanium Dioxide, E. Merck, 64271 Darmstadt, Germany), NaCl powder, and distilled water. The method used to produce test sample is by mixing all the ingredients to obtain a homogeneous test sample. The test sample consists of two variations, namely variations in the composition of glycerin and variations of TiO_2. There were several steps taken to get the sample. First, 3 grams of powdered gelatin and 10 ml of saline were mixed. Alloy gelatin and saline solution can be obtained by homogeneous stirring at 35°C to 40°C for 35 minutes or until the solution becomes homogeneous. Then glycerin with concentrations of 85%, 90%, 95%, and 100% was added to the homogenized solution of gelatin, as shown in Table 1. The ratio for gelatin solution: glycerin is 3: 1 (v / v). The gelatin solution and glycerin were mixed for 10 minutes and stirred at 35°C - 40°C. Next, the sample was poured into four 40 ml plastic pot-shaped cylinder with a diameter of 36 mm. The fourth test sample was placed in the room temperature (T = 27°C) for several days, then its durability properties were observed. After obtaining the most durable test samples, the second variation was done which was the addition of TiO_2 variation of 0.01 grams - 0,025 grams. TiO_2 mixing process took about 60 minutes. Then the sample was poured into a cylindrical plastic pot with a diameter of 27 mm.

The structure of TiO_2 was determined by conventional X-ray diffraction (Philips PW 1820 powder

diffractometer with an accuracy of 0.0158 in 2θ using CuKa radiation). The characterization of the samples was done by doing the physical characterization test, the FTIR test, the DSC test, the materials homogeneity test and the material absorption coefficient (μ_a) test. The physical characterization was performed to determine the durability and the modulus of elasticity, so that samples can be used optimally. Gelatin is not stable in aqueous solvent systems and undergoes a progressive hydrolytic degradation lowering its molecular weight and consequently decreasing useful physical properties. Hydrolysis of the gelatin depends on the temperature, pH of the system and to a lesser extent on the nature of the other solutes that can be present. The activity of fungi is to break the polymer chains of gelatin and use it to grow and affect the physical characteristics of the samples. This test was used to observe the durability of the samples towards the environment. The durability test was performed in an open room at room temperature. The preservation period was measured from the setting of the sample to the growth of fungi in the sample. The pressure test was performed to analyse the sample's modulus of elasticity. The FTIR test was performed to determine the functional groups of each ingredient. The DSC test was carried out on the effect of temperature on test material to ensure that during the tomographic test, the sample was not degraded due to the heat radiation of the laser. The next test was the homogeneity and optical properties test which was performed by measuring the absorption coefficient value ($\searrow_a$) of samples by using homemade continuous wave diffuse optical tomography, CWDOT (Ukhrowiyah, 2015). In measuring the absorption coefficient value ($\searrow_a$), the sample with TiO_2, was made by five thickness variations including 4 mm, 8 mm, 12 mm, 16 mm and 20 mm.

3. RESULTS AND DISCUSSION

3.1. Result of Physical Characterization Test

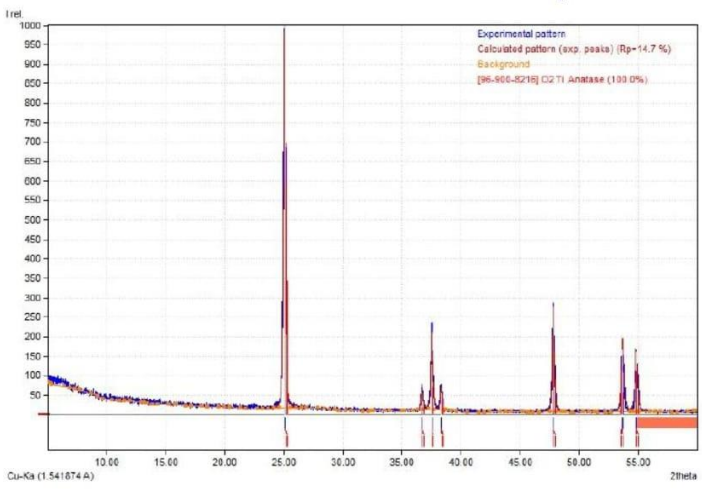

Fig 1. Diffractogram of TiO_2

The XRD pattern was recorded at the angular range of $2\theta = 5° - 60°$. Figure 1 shows the X-Ray diffractometry, which indicates that the structure of TiO_2 is anatase phase, indexed by JCPDS card no. 96-900-8261, the strongest peak is (101). The UV-Vis spectroscopy identification that TiO_2 increased absorption is shown in Figure 2 and Table 1. XRD test and UV/Vis Test showed that the addition of TiO_2 enhance the absorbance of the sample for all wavenumbers, especially at 780 nm, 808 nm, and 830 nm.

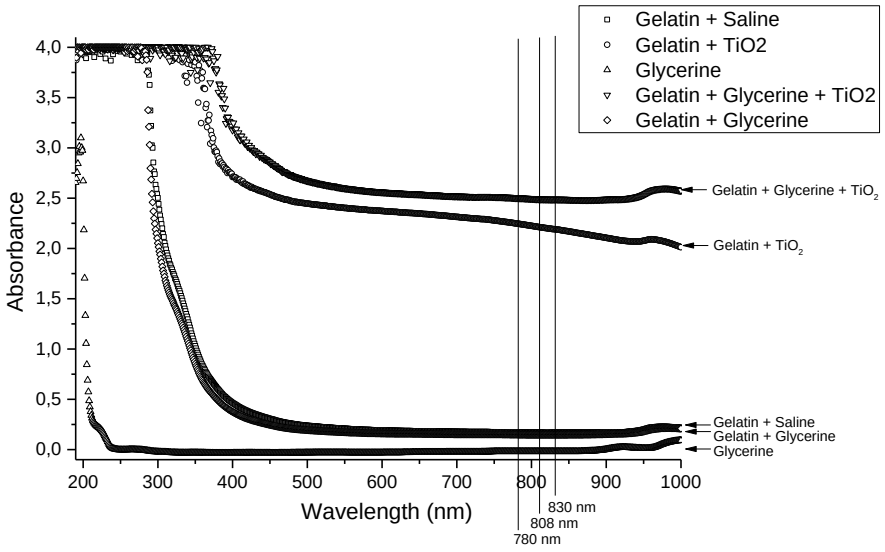

Figure 2. UV-Vis spectrogram of samples of glycerin, gelatin-glycerin, gelatin-saline, Gelatine-TiO_2, gelatin-glycerin-TiO_2

Table 1. Absorbance of Samples glycerin, gelatin-glycerin, gelatin-saline, Gelatine-TiO_2, gelatin-glycerin-TiO_2

Wavelength (nm)	Absorbance				
	Gelatin + Saline	Gelatin + TiO_2	Glycerine	Gelatin + Glycerine + TiO_2	Gelatin + Glycerine
780	0.172	2.248	-0.02	2.504	0.15
808	0.169	2.215	-0.019	2.494	0.147
830	0.169	2.192	-0.019	2.489	0.148

3.2. Result of Physical Characterization Test

The synthesis result of gelatin-glycerin composite samples is shown in Figure 3. Figure 3A shows the samples of gelatin-glycerin sample without TiO_2 while Figure 3B shows the samples of gelatin-glycerin which was added by TiO_2. The gelatin-glycerin sample without TiO_2 was tested for its durability. The observations were done at room temperature (29.7°C) and air humidity of 57% to know the growth of fungi. Table 1 shows data of durability test on the concentration variations of glycerin used. Whereas, the presence of fungi that grew in the sample is shown in Figure 4.

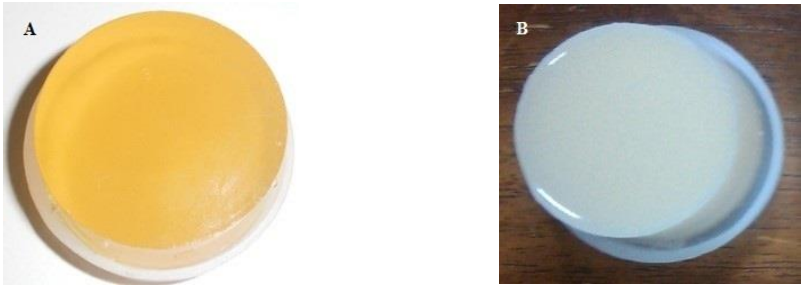

Figure 3. Gelatin-glycerin samples (a) without the addition of TiO_2 (b) the addition of 0.01 grams TiO_2

Table 2. Durability Test Results of Gelatin-glycerin Phantom at room temperature (27°C)

Type of sample	Variation of Glycerin Concentration (%)	Preservation (Hour)
A	85	108
B	90	108
C	95	72
D	100	126

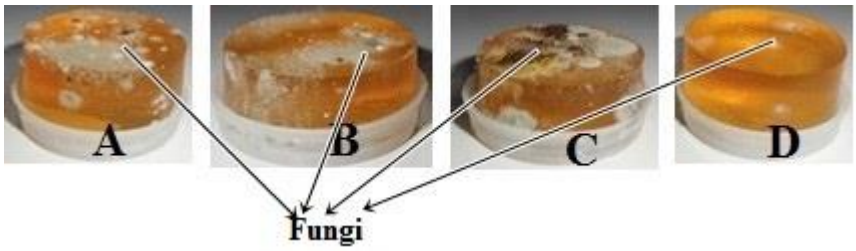

Figure 4. Durability Test Results of Gelatin-glycerin Samples at 27°C

Based on the Table 2, it can be seen that the higher the concentration of glycerin, the more durable sample. Samples with addition of glycerin with concentration of 100% could last for 126 hours. It is also shown that in the sample D, the number of fungi found is the least. The most durable sample (D) was used for calibration of NIR-DOT via homogeneity test and material absorption coefficient (μ_a) test. Its sample was added TiO_2 at different concentrations, as shown in Figure 3B. Even though, there was a decrease on Sample (C), the trend of the durability is increase when the concentration of glycerin is increase as well.

The second physical characterization determines the modulus of elasticity. The test was done by pressuring the sample with force measurement device (IMADA). The result of the test is shown in Table 3 and Figure 4. Based on Table 3 and Figure 5, it can be shown that the higher the glycerin concentration added to the gelatin solution, the lower the modulus of elasticity. The elastic modulus values of the four samples are still higher compared to the value obtained by the previous researches whose magnitude was between 0.167 KPa and 29 KPa (Mc Kee, 2011).

Table 3. Result of compressive strength test analysis.

Sample	Concentration of Glycerin (%)	Force, F (N)	Modulus Elasticity, E (KPa)
A	85	44.32	80.29 ± 5.70
B	90	30.75	61.01 ± 4.61
C	95	29.2	66.12 ± 7.57
D	100	22.03	45.89 ± 3.58

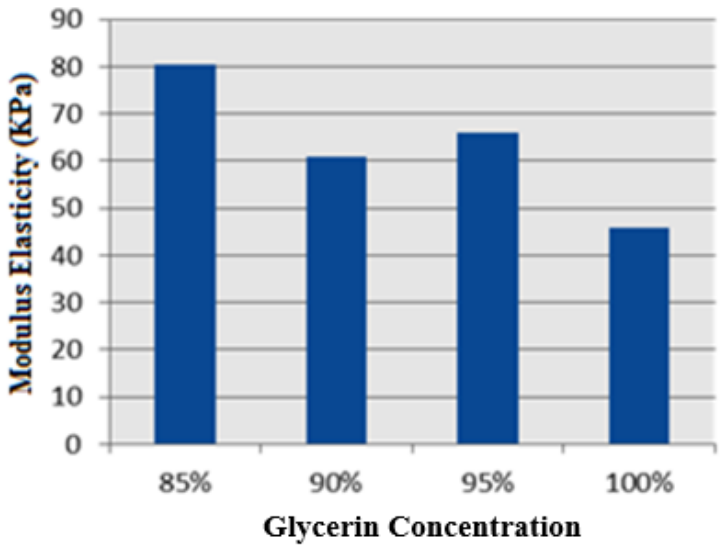

Figure 5. Graph on relationship between the elasticity modulus of gelatine–glycerin with concentration glycerin

3.3. Result of FTIR Test

The FTIR characterization test results performed on samples of gelatine, glycerin, gelatine-glycerin, and gelatine-glycerin-TiO_2 are shown in Figure 6. The FTIR analysis was conducted by matching the wave absorption unique area to each functional group. Results of functional groups along with local uptake obtained by FTIR spectra are shown in Table 4.

Table 4 shows that the typical functional group of gelatin, namely N-H, still appears on FTIR of gelatin-glycerin sample and gelatin-glycerin-TiO_2 phantom spectra. In addition, the typical functional group of glycerin, namely C-OH (primary alcohol and secondary alcohol), also appears.

Table 4. Results of FTIR Spectrum Analysis

Functional Group	**Wave Number (cm^{-1})**			
	Gelatin	**Glycerin**	**Gelatin-Glycerin 100%**	**Gelatin-Glycerin 100%-TiO_2 0,025 g**
Stretching Vibration OH (bending H intermolecular)	3398.69	3396.6	3406.4	3396.76
Stretching Vibration C-H	-	1641.48	-	1647.26
Stretching Vibration C-OH (*primary alcohol*)	-	1111.03	1111.03	1111.03
Stretching Vibration C-OH (*secondary alcohol*)	-	1043.52	1043.52	1043.52
Bending Vibration N-H	1656,91	-	1651.12	1647.26
Deformation Vibration N-H	1545,03	-	-	-
Fuctional group of carboxyl COO^-	1336,71	-	-	-
Stretching Vibration C=O	-	1641.68	1651.12	1647.26
Vibration C=N	-	-	-	-

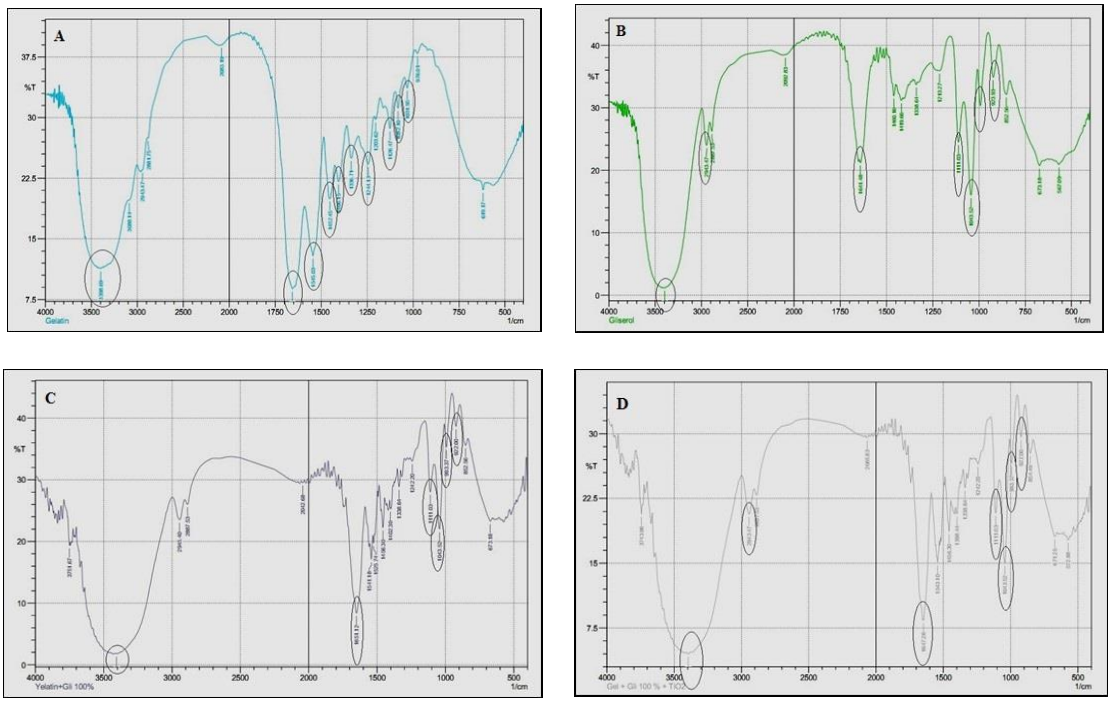

Figure 6. FTIR spectra of (A) gelatin, (B) Glycerin, (C) gelatin-glycerin, and (D) gelatin-glycerin-TiO_2.

Figure 6A shows the FTIR spectrum of gelatin. This spectrum shows the gelatin typical functional group absorption area at wavenumber 3398.69 cm^{-1} which is a stretching vibration of OH (intermolecular H bond). The intermolecular H bond is a strong absorber at a wavelength 3398.69 cm^{-1} and has sharp peaks. This indicates the purity level of gelatin. In the region of wave number 1656.91 cm^{-1}, there was an absorption of bending N-H functional group. The N-H function group is a typical functional group of gelatin. The area of wavenumber absorption of 1545.03 cm^{-1} and 1452.45 cm^{-1} is the N-H deformation vibration and C-H deformation vibration (Mistry, 2009). Wave number 1336.71 cm^{-1} is the absorption area of carboxyl (COO-) proline gelatin which is the characteristic of type 1 collagen.

Figure 6B represents the FTIR spectrum of glycerin or glycerol. Glycerin is an alcohol derivative that has several spectra of typical absorption regions. The absorption area at wavenumber of 3396.76 cm^{-1} is the absorption of stretching functional group OH (intermolecular H bond). At wavenumber 2943.47 cm^{-1}, there was absorption of C-H stretching functional groups. Wavenumber 1641.48 cm^{-1} is the absorption area of the functional group C = O (intermolecular H bond). Wavenumber 1111.03 cm^{-1} is the absorption of stretched C-OH functional group. The C-OH function group is one of the functional groups of primary alcohol (Mistry, 2009). The absorption area at wavenumber 1043.52 cm^{-1} is the absorption of the C-OH functional group (secondary alcohol) stretching vibration.

Figure 6C shows the results of the FTIR spectrum of gelatin-glycerin sample (sample D). Based on the spectrum produced, there are several absorption areas that are characteristic of the main ingredients used, such as the wavenumber 3406.4 cm^{-1} which is an OH functional group (intermolecular H bond) of all the main ingredients that have OH functional groups. In the FTIR spectrum, wavenumber 1651.12 cm^{-1} is the absorption area of the functional group C = O, the curve vibration which is a characteristic of primary amide uptake. The primary amide functional group is a typical functional group of gelatin. Wavenumbers 1111.03 cm^{-1} and 1043.52 cm^{-1} are absorption areas of stretching vibration of C-OH functional groups which are characteristic of glycerin namely primary alcohol and secondary alcohol.

Figure 6D shows the results of FTIR spectrum of gelatin-glycerin-TiO_2 sample (sample D which is added 0.025 g TiO_2). Based on the resulting spectrum, there are several absorption areas that show the characteristics of the main materials of gelatin and glycerin. The OH (intermolecular) functional group absorbs at wavenumber 3396.76 cm^{-1} which experienced a shift from the main material absorption area before mixing. At wavenumber 1647.26 cm^{-1}, the typical functional group of gelatin is the functional group C = O the buckling vibration also still appeared. Similar to the gelatin characteristic absorption area, at wavenumbers 1111.03 cm^{-1} and 1043.52 cm^{-1}, in the area of absorption of C-OH functional groups curvature vibrations (primary alcohol and secondary alcohol) which are characteristic of glycerin, also still appeared.

3.4. *Result of Differential Scanning Calorimetric Test (DSC)*

The DSC test in this study aimed to determine the acceptable temperature of samples so that the samples are not degraded when they are irradiated by the laser. In this DSC test, sample D was used and heated in 40-70^oC temperature range, and the temperature increment was 5°C per minute. Temperatures used in the DSC test were based on the characterization of laser in which laser output generates temperature of 20^oC every 10 minutes and the test process was performed for ± 10 minutes for one sample. The thermogram of synthesized gelatine-GA-TiO_2 is shown in Figure 7.

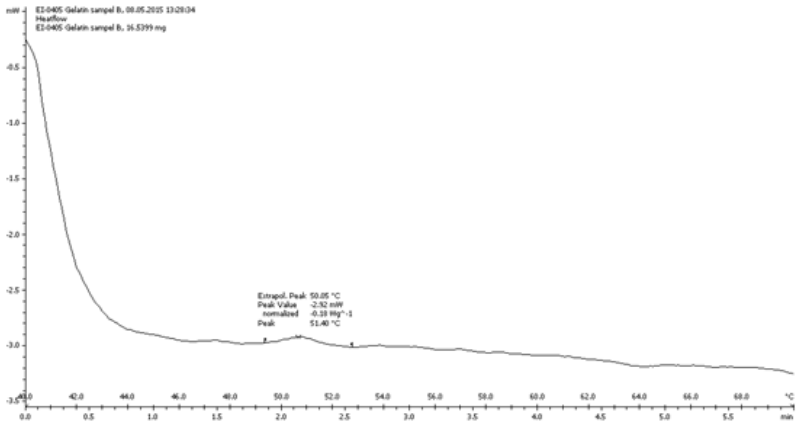

Figure 7. DSC thermogram gelatine-glycerin-TiO_2

Based on the graph in Figure 7, characterization results showed that there was no change in physical reaction in the sample. This was indicated by the absence of melting points, glass transition, and crystallinity at 40°C - 70°C. Based on these results, gelatin-glycerin-TiO_2 phantom, which was given a direct exposure at 40°C - 70°C, did not experience exothermic reactions or endothermic reactions. The main ingredients, gelatin has a melting point at 30°C to 40°C while TiO_2 has a melting point at 1855°C. The addition of TiO_2 to the gelatin-glycerin sample can increase resistance to its thermal characteristics. This indicates that the gelatin-glycerin-TiO_2 phantom can be applied optimally as a breast phantom without concerns of any exothermic or endothermic reactions due to changes in temperature.

3.5. Result of Homogeneity Test

The homogeneity test was conducted to determine the homogeneity of gelatine-glycerin-TiO_2 phantom. In this test, the sample D was added by TiO_2 with variations of 0.01; 0.015; 0.02 and 0.025 gram. The laser with 3 variations of NIR wavelengths, which are 780 nm, 808 nm and 830 nm, were incorporated to this sample by using CWDOT. Figure 8 shows the relationship between output Voltage (V) to source position for sample D +TiO_2 0.025 gram at wavelengths of 780 nm, 808 nm and 830 nm. The sample will have a good homogeneity, if the position between sources that have the same distance to the detector produce the same output voltage. Under these conditions, the graph of the output voltage generated by the source position has a trend line or a U-shaped pattern. Based on Figure 8, it can be seen that all wavelength variations have a trend line or a similar U-shaped pattern.

Based on Figure 8, the optical output voltage at λ = 808 nm generates maximum value. However, the power generated by the wavelength of 808 nm is too big (180 mW). One of advantages of DOT in the diagnosis of breast cancer is that the laser source used is a low-power laser that is safe and non-invasive in analyzing the internal structure of human tissue. Therefore, the light source with λ = 808 nm (180 mW) is not suitable to be used in the diagnosis of breast cancer. Based on this analysis, the absorption coefficient test used λ = 830 nm because it has much lower power (30 mW).

Figure 9 shows the relationship between transmitted intensity of laser after passing samples as a.function mass of TiO_2 at wavelengths of 780 nm, 808 nm and 830 nm. Output voltage value was generated by the sample with the addition of 0.025 grams TiO_2 which yields its minimum value. Output voltage (V) accounts for the transmitted laser intensity after passing through the sample, the smaller the value of the optical output voltage, the greater the intensity absorbed by the sample. The position number DOT laser source device was selected at the 9th position because it is the furthest from the source. Based on the results shown in Figure 9, the absorption coefficient test was carried out on samples with the addition of 0.025 grams TiO_2. Laser with λ = 808 nm showed a decrease in the value of the output voltage that is significant compared to the value of the output voltage at λ = 780 nm and λ = 830 nm, but the generated power was too big (180 mW), so that the coefficient test absorbency used laser with λ = 830 nm, which generated 30 mW.

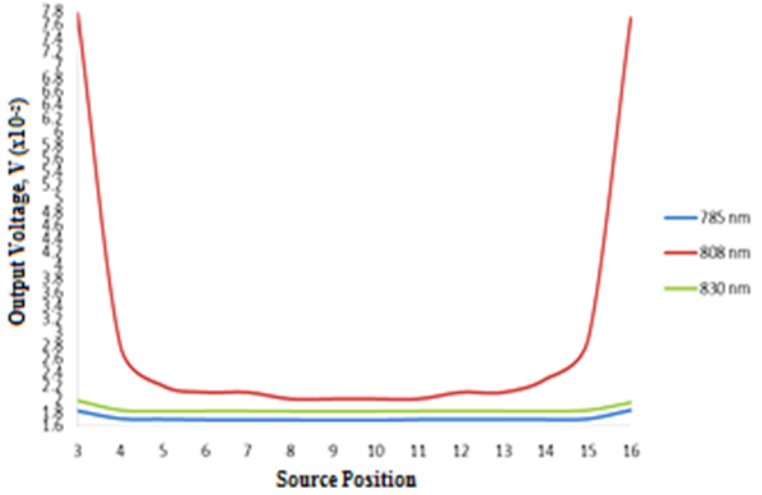

Figure 8. The relationship between output voltage (V) to source position for Sample D + 0.025 gram TiO_2 at wavelengths of 780 nm, 808 nm and 830 nm.

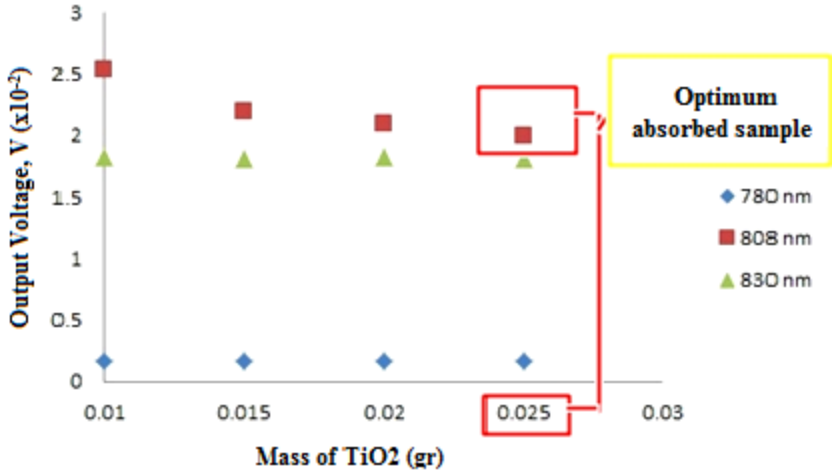

Figure 9. Relationship between transmitted intensity of laser after passing samples as a function mass of TiO_2

3.6. Result of Absorption Coefficient Test

Figure 10 shows the relationship between transmitted intensity of laser after passing samples as function sample thickness. The absorption coefficient test was only performed on the sample with gelatin-glycerine-TiO_2 since the gelatin-glycerin sample was a transparent material. The absorption coefficient test results showed that the exponential function equation is $y = 0.365\ e^{-0.167x}$. The function y represents a value of intensity (I) and the

function x represents a value of thickness sample. Based on the Lambert-Beer law, the absorption coefficient (μa) of gelatin-glycerin-TiO_2 phantom at wavelength of 830 nm is 0.167 mm^{-1}. This value corresponds to the absorption coefficient (μ_a) breast at NIR wavelength of 0.1 - 1 mm^{-1} (Hielscher, 2002).

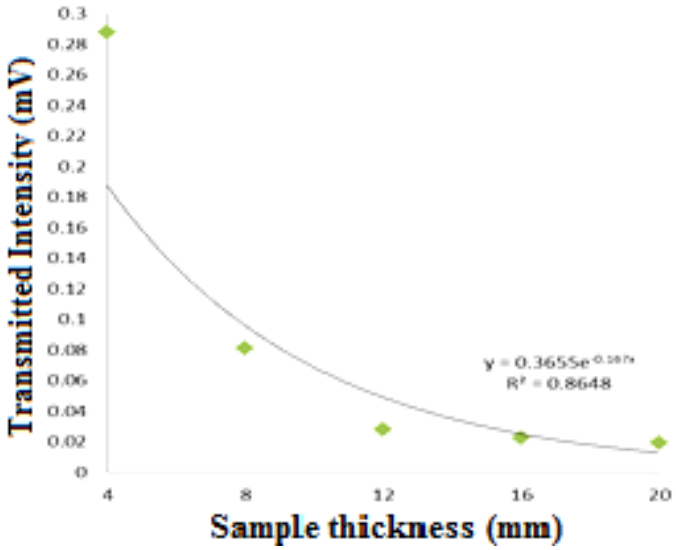

Figure 10. Relationship between transmitted intensity of laser after passing samples as a function sample thickness.

4. CONCLUSION

The addition of glycerin in gelatin based phantom composites can increase the durability of the sample. The higher concentration of glycerin added, the more durable the sample are. The most durable sample can be obtained from the addition of glycerin concentration of 100%, which was for 126 hours. The addition TiO_2 in gelatin – glycerin sample cause gelatin – glycerin sample as the diffuse material. The optimum sample was achieved at wavelength of 830 nm with TiO_2 variation of 0.025 grams. When NIR laser with wavelength of 830 nm and 30 mW power exposure on this sample, generates the absorption coefficient of 0.167 mm^{-1}. The breast tissue is a diffuse material with absorption coefficient (μ_a) at NIR wavelength of 0.1 - 1 mm^{-1}. So, phantom based on gelatin-glycerin-TiO_2 can be applied as material replacement of breast for test object in CW-DOT.

5. ACKNOWLEDGEMENT

The authors would like to express their gratitude to the DGHE of Indonesian Government for the support through Universitas Airlangga Research Grant (No. 200/UN3.14/LT/2018).

6. REFERENCES

Azamris (2006) Analisis Faktor Risiko Pada Pasien Kanker Payudara di RS M. Djamil Padang, *Jurnal Cermin Dunia Kedokteran* 152:53-6.

De Grand A.M., Lomnes S.J., Lee D.S., *et al*. (2006) Tissue-like phantoms for near-infrared fluorescence imaging system assessment and the training of surgeons, J. Biomed Opt. 2006;11(1):014007.

Heilscher, A.H, A.Y. Bluestone, G.S. Abdoulaev, A.D. Klose, J. Lasker, M. Stewart, U. Netz, dan J. Beuthan (2002) Near-infrared diffuse optical tomography, *Disease Markers,* 18 (313-337).

Jiang, S., Pogue, B.W., Mc. Bride, T.O., Paulsen, K.D. (2003) Quantitative analysis of near-infrared tomography: sensitivity to the tissue-simulating precalibration phantom, *J. Biomed Opt*. 8 (2), 308-315.

Kemsley E. Kate, Henri S. Tapp, Richard Binns, Robert O. Mackin, Anthony J. Peyton (2008) Feasibility study of NIR diffuse optical tomography on agricultural produce, Journal of Postharvest Biology and technology 48223-230.

Lualdi M., Colombo A., Farina B. and Tomatis S., Marchesini R. (2001) A phantom with tissue-like optical properties in the visible and near infrared for use in photomedicine, *Lasers in Surgery and Medicine* Vol. 28.

McKee, C. T. (2011), Indentation Versus Tensile Measurements of Young's Modulus for Soft Biological Tissues, *Tissue Engineering*, Part B Volume 17.

N. Ukhrowiyah, D. Kurniadi, Suhariningsih, M. Yasin (2015) Continuous Wave Diffuse Optical Tomography Using Multimode Plastic Fiber for Non-destructive Test of Diffused Material, Optoelectronic and Advanced Material-Rapid Communication,Vol. 9, No. 7-8, p. 995 - 999

Pogue, B.W. and M.S. Patterson (2006) Review of tissue simulating phantoms for optical spectroscopy, imaging and dosimetry, *J Biomed Opt.* 11(4): p. 041102.

Riset Kesehatan Dasar (2013) Badan Penelitian dan Pengembangan Kesehatan, *Kementrian Kesehatan RI*, p 38.